Joule

CellPress

Article

High Performance Printed AgO-Zn Rechargeable Battery for Flexible Electronics

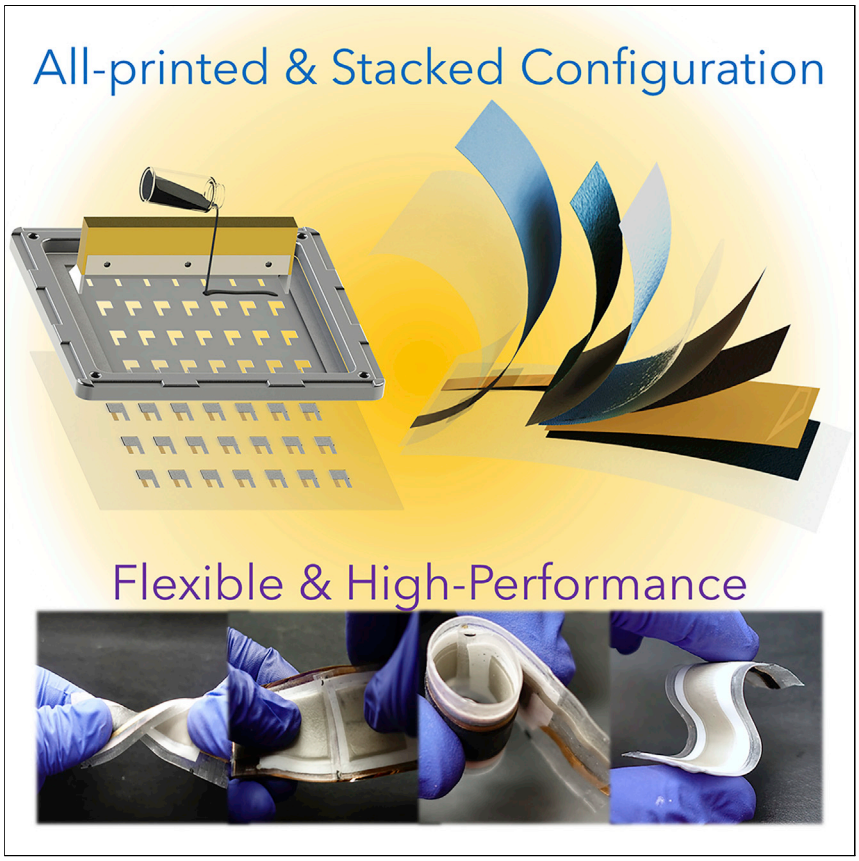

This work describes a screen-printable polymer composite AgO-Zn battery that features high flexibility, rechargeability, high areal capacity, and low impedance. The battery has reached the highest areal capacity to date of 54 mAh/cm^2 for primary applications. It is durable under repeated deformation, rechargeable, and completely customizable in different sizes and areal capacities, allowing for powering flexible electronic and display systems with Bluetooth and microcontroller components that demand high peak power.

Lu Yin, Jonathan Scharf, Jessica Ma, ..., Xia Wei, Joseph Wang, Ying Shirley Meng

josephwang@ucsd.edu (J.W.)
shmeng@ucsd.edu (Y.S.M.)

HIGHLIGHTS

Novel polymer-based screen-printing of battery with a high areal density of 54 mAh/cm^2

A battery featuring flexibility, rechargeability, low impedance, and customizability

Superior battery performance in pulsed high current discharge mode

Yin et al., Joule 5, 1–21
January 20, 2021
https://doi.org/10.1016/j.joule.2020.11.008

Please cite this article in press as: Yin et al., High Performance Printed AgO-Zn Rechargeable Battery for Flexible Electronics, Joule (2020), https://doi.org/10.1016/j.joule.2020.11.008

Joule

CellPress

Article

High Performance Printed AgO-Zn Rechargeable Battery for Flexible Electronics

Lu Yin,[1,4] Jonathan Scharf,[1,4] Jessica Ma,[1] Jean-Marie Doux,[1] Christopher Redquest,[1] Viet L. Le,[1] Yijie Yin,[1] Jeff Ortega,[3] Xia Wei,[3] Joseph Wang,[1,2,*] and Ying Shirley Meng[1,2,5,*]

SUMMARY

The rise of flexible electronics calls for cost-effective and scalable batteries with good mechanical and electrochemical performance. In this work, we developed printable, polymer-based AgO-Zn batteries featuring flexibility, rechargeability, high areal capacity, and low impedance. Using elastomeric composites, the current collectors, electrodes, and separators can be fabricated via a high-throughput, scalable, and layer-by-layer screen-printing process and vacuum-sealed in a stacked configuration. The batteries are customizable in sizes and capacities, with the highest obtained areal capacity of 54 mAh/cm^2 for primary applications. Advanced X-ray tomography, impedance spectroscopy, and rigorous deformation tests were used to characterize the battery. The batteries were used to power a flexible E-ink display system that requires a high-current drain and exhibited superior performance compared to commercial lithium coin cells under the same pulsed-discharge conditions. The developed battery presents a practical solution for powering a wide range of electronics and holds major implications for the future development of high-performance flexible batteries.

INTRODUCTION

Recent interest in multifunctional flexible electronics for applications in sensing, displays, and wireless communication advocates for the development of complementary flexible energy storage solutions.[1,2] Accordingly, numerous efforts have been made to tackle the challenges of fabricating batteries with robust mechanical resiliency and high electrochemical performance. To do so, several studies focused on adapting novel battery fabrication techniques, such as substrate pre-stretching, textile-embedding, and "island-bridge," wire, cable, kirigami, and origami structuring to endow structural flexibility and stretchability to batteries.[3–9] Other studies focused on tackling the challenge by the means of material innovation, developing polymer-based current collectors, electrodes, separators, and electrolytes for various intrinsically flexible and stretchable batteries.[10–17] However, due to the exponential growth in the wearable flexible electronics market, manufacturers started to realize the urgent need for scalable, low-cost, and high-performance flexible battery technologies to provide practical energy storage solutions for the tens of millions of devices produced every year. Many flexible batteries rely on fabrication processes that are complex, low throughput, and high cost and thus have limited practicality which hinders their lab-to-market transformation. Addressing the need for flexibility and scalability while maintaining low cost, printed high-performance batteries are crucial for realizing most of the commercially viable battery technology. Using low-cost thick-film fabrication technologies, flexible battery components can

Context & Scale

The next-generation wearable sensors and electronics require batteries that are safe, flexible, high energy density, and low impedance to enable functionalities with high power demand. However, traditional batteries are limited in safety and flexibility, and existing flexible batteries are limited in capacity, peak performance, and production throughput. Addressing such limitations, this work reports the development of an all-printed, flexible, and rechargeable AgO-Zn battery that features both robust mechanical resiliency and high electrochemical performance. Using polymer-based composite inks, the current collectors, electrodes, and separators of the battery can be screen-printed to obtain areal capacities up to 54 mAh/cm^2. Such AgO-Zn batteries exhibit superior performance over lithium coin cells in powering high current and flexible electronic systems and present major implications for the future development of printed batteries and the development of the flexible electronics market.

be printed sheet-to-sheet or roll-to-roll using traditional, low-maintenance screen-printing or doctor-blade-casting equipment, thus realizing low-cost mass production of flexible batteries.[18]

Among many commercialized printed flexible batteries, aqueous zinc (Zn)-based conversion cells were successful in developing products with high throughput and low production cost.[19] The Zn anode chemistry has been of special interest for the flexible battery market due to its low material cost, high theoretical capacity (820 mAh/g, 5,854 Ah/L), good rechargeability, and safe chemistry.[20,21] In addition, as Zn and the aqueous electrolyte can be readily handled in an ambient environment, the equipment and production costs of Zn-based batteries are often considerably lower compared to that of lithium (Li)-ion batteries. However, commercial Zn-based printed flexible batteries are usually non-rechargeable and feature low capacity and high impedance, thus limiting their application in low-power, disposable electronics only. Addressing these limitations, several studies have reported the development of printable, rechargeable, and high-performance Zn-based batteries.[16,22,23] Among them, the silver(I) oxide-zinc (Ag_2O-Zn) battery has attracted particular attention due to its rechargeable chemistry and its tolerance to high-current discharge.[24,25] The redox reaction relies on the dissolution of zinc ions (Zn^{2+}) and silver ions (Ag^{+}) in the alkaline electrolyte and their supersaturation-induced precipitation, which takes place rapidly while maintaining a stable voltage at 1.56 V (Equations 1, 2, 3, 4, 5, and 6).[26,27] All E° potentials are indicated using the standard hydrogen electrode (SHE) as a reference.

Anode:

$$\text{(Dissolution)}\quad Zn(s) + 4OH^{-}(aq) \leftrightarrow Zn(OH)_4^{2-}(aq) + 2e^{-} \qquad \text{(Equation 1)}$$

$$\text{(Relaxation)}\quad Zn(OH)_4^{2-}(aq) \leftrightarrow ZnO(s) + H_2O + 2OH^{-}(aq) \qquad \text{(Equation 2)}$$

$$\text{(Overall)}\quad Zn(s) + 2OH^{-}(aq) \leftrightarrow ZnO + H_2O + 2e^{-} \quad E^{\circ} = -1.22 \text{ V versus SHE} \qquad \text{(Equation 3)}$$

Cathode:

$$\text{(Dissolution)}\quad Ag + OH^{-} \leftrightarrow AgOH(aq) + e^{-} \qquad \text{(Equation 4)}$$

$$\text{(Relaxation)}\quad 2AgOH(aq) + 2OH^{-} \leftrightarrow Ag_2O(s) + H_2O \qquad \text{(Equation 5)}$$

$$\text{(Overall)}\quad Ag_2O(s) + H_2O \leftrightarrow 2Ag(s) + 2OH^{-}(aq) \quad E^{\circ} = +0.34 \text{ V versus SHE} \qquad \text{(Equation 6)}$$

Most of these batteries rely solely on the use of the lower oxidation state of silver to obtain reversible redox reaction, whereas the higher oxidation state (AgO), with its redox reaction described in Equation 7, has been rarely utilized.

$$2AgO(s) + H_2O + 2e^{-} \leftrightarrow Ag_2O(s) + H_2O(l) \quad E^{\circ} = +0.60 \text{ V versus SHE} \qquad \text{(Equation 7)}$$

The underutilization of AgO can be attributed to its instability, namely, its lattice phase change when transitioning into Ag_2O, which may result in irreversible shape changes that impede rechargeability, and its high charging potential responsible for possible electrode gassing due to oxygen evolution reaction.[8,28–31] However, once addressing these issues, it is possible to access a much higher theoretical cathode capacity (from 231 mAh/g for Ag_2O to 432 mAh/g for AgO). So far, printed Ag-Zn batteries reported in the literature still have low rechargeability (<50 cycles),

[1]Department of Nanoengineering, University of California, San Diego, La Jolla, CA 92093, USA

[2]Sustainable Power and Energy Center (SPEC), University of California, San Diego, La Jolla, CA 92093, USA

[3]ZPower LLC, Camarillo, CA 93012, USA

[4]These authors contributed equally

[5]Lead Contact

*Correspondence: josephwang@ucsd.edu (J.W.), shmeng@ucsd.edu (Y.S.M.)

https://doi.org/10.1016/j.joule.2020.11.008

Please cite this article in press as: Yin et al., High Performance Printed AgO-Zn Rechargeable Battery for Flexible Electronics, Joule (2020), https://doi.org/10.1016/j.joule.2020.11.008

limited capacity (<12 mAh/cm^2 for primary cell, <3 mAh/cm^2 for secondary cell), along with high internal resistance (~10^2 Ω) that results in large voltage drop during operation.[10,29,32–34] Such limitations are hindering the adaptation of Ag-Zn printed batteries in flexible electronics.

Herein, we present a novel fabrication process of all-printed, flexible, and rechargeable AgO-Zn batteries with ultra-high areal capacity, low impedance, and good rechargeability as a practical energy storage solution for flexible electronics. The fabrication of the cell relies on low-cost, high-throughput, layer-by-layer printing of formulated powder-elastomer composite inks to form the current collectors, Zn anode, AgO cathode, and their corresponding separators. The battery adopts a low-footprint stacked configuration, with potassium hydroxide (KOH) - poly(vinyl alcohol) (PVA) hydrogel as a low impedance electrolyte sandwiched between the 2 fully printed electrodes. Using the thermoplastic styrene-ethyl-butylene-styrene block copolymer (SEBS) elastomer-based substrate, the assembled battery can be directly heat- and vacuum-sealed to preserve the electrolyte and ensure appropriate cell pressure during operation. This fabrication and assembly process can be applied to different cell sizes with adjustable areal capacity, allowing customizable battery form factors that are tailored for specific applications. Fully utilizing the higher oxidation state of the AgO, the as-printed cells were able to reach a high areal capacity of >54 mAh/cm^2 while maintaining a low internal resistance (~10 Ω) for primary applications. Furthermore, utilizing an optimized cycling profile, the printed cells were recharged for over 80 cycles, sustaining 0.2–1 C discharges without exhibiting significant capacity loss while maintaining low impedance throughout each cycle. Moreover, the fabricated cells displayed outstanding robustness against repeated bending and twisting deformations. To demonstrate their performance in powering typical flexible electronics, the fabricated batteries were successfully implemented in a flexible E-ink display system with an integrated microcontroller unit (MCU) and Bluetooth modules that require pulsed high-current discharge. Leveraging a low-cost scalable production process, polymer-based flexible architecture, and customized ink formulations, the all-printed AgO-Zn battery, with its desirable mechanical and electrochemical performance, presents a practical solution for powering the next-generation flexible electronics and sets a new benchmark for the further development of printable flexible batteries.

RESULTS

All-Printed Polymer-Based Fabrication

The all-printed fabrication of the flexible AgO-Zn battery was designed based on the careful selection of elastomers for the substrate, sealing, and ink binders based on their mechanical properties, chemical stabilities, and processabilities. SEBS was selected as the substrate material owing to its good solvent processability, chemical stability under high pH, outstanding elasticity, as well as appropriate melting point (~200°C), allowing it to be easily cast into films that are chemically stable, flexible, and heat-sealable to support and seal the battery.[35] Screen-printing, a low-cost high-throughput thick-film technique was used for ink deposition, as it allows the efficient fabrication of the current collectors, electrodes, and separators into their preferred shapes and thicknesses.[18] The screen-printing of the batteries relies on the customized formulation of 6 inks corresponding to the current collectors, electrodes, and the separators for both the anode and cathode. Conductive and flexible silver ink and carbon ink were printed as the anode and cathode current collectors, respectively. Both inks use SEBS as the elastomer binder and toluene as the solvent to allow the ink to firmly bond to the toluene-soluble SEBS substrate. The anode ink

Please cite this article in press as: Yin et al., High Performance Printed AgO-Zn Rechargeable Battery for Flexible Electronics, Joule (2020), https://doi.org/10.1016/j.joule.2020.11.008

is composed of Zn particles with bismuth oxide (Bi_2O_3) as an additive to reduce dendrite formation and suppress H_2 gassing, whereas the cathode ink is mainly composed of AgO powder with a small amount of lead oxide coating to enhance the electrochemical stability and carbon black added to enhance the electronic conductivity of the electrode.[29] A high-pH stable, elastomeric fluorocopolymer was used as the binder for both electrodes owing to its solubility in lower ketones, which is less prone to oxidation by the highly oxidative AgO. Cellulose powder was used to form the porous cathode separator that mimics the use of cellophane to capture and reduce dissolved silver ions (Ag^+) and prevent material crossover.[8,19] A titanium-dioxide (TiO_2)-based ink was formulated for the anode separator, acting as a physical barrier to Zn dendrite growth. The inclusion of TiO_2 also aids the recrystallization of zincate, hence preventing the Zn from traveling toward the cathode. Finally, a solid-phase polyvinyl alcohol (PVA) hydrogel crosslinked with potassium hydroxide (KOH) was prepared as the electrolyte, which complements the cell flexibility without the risk of leaking. Lithium hydroxide (LiOH) and calcium hydroxide ($Ca(OH)_2$) were used as additives in the electrolyte to maintain electrolyte chemical stability and minimize Zn dissolution, which in turn prevents the uncontrolled recrystallization of Zn during charging that leads to dendrite growth.[36,37]

The fabrication of the batteries begins with the preparation of the substrates, where a resin of SEBS dissolved in toluene was casted onto wax papers using film casters and dried in the oven to form a transparent elastic film. The layer-by-layer printing process is illustrated in Figure 1A. First, the Ag and the carbon inks were printed onto the SEBS substrate as current collectors, with a 400 nm layer of gold sputtered onto the carbon current collectors to enhance their conductivity and chemical stability. Then, the Zn and the TiO_2 inks, and the AgO and the cellulose inks were printed onto their corresponding current collectors. To complete the cells, the KOH-PVA hydrogel electrolyte was cut to size and sandwiched between the 2 electrodes. Finally, the casing of batteries was heat and vacuum sealed and separated into individual cells, finalizing the scalable sheet-by-sheet fabrication of multiple cells in one sitting. The flexible, vacuum-sealed AgO-Zn batteries comprising 9 layers of composite materials can thus be easily fabricated using layer-by-layer screen-printing (Figure 1B). The major advantage of the stencil printing technique is the customizable dimension of the cells that can be tailored for different applications with specific form factor and capacity requirements. As examples, cells in different sizes were fabricated using the same fabrication process (Figure 1C) and could be integrated with different sizes of flexible electronic devices. Regardless of the shapes and sizes, the assembled cells are highly flexible and durable under repeated mechanical deformations (Figure 1D), making them highly suitable for powering wearable and flexible electronics that require high resiliency to various deformations. Furthermore, the superior electrochemical performance of the fabricated AgO-Zn battery greatly expands the application of flexible printed batteries in electronics with high power demands. This capability was demonstrated by powering a flexible display system with microcontroller and Bluetooth modules (Figure 1E), as discussed in the later section.

Microstructural and Electrochemical Characterization

The printed electrodes and separators (Figure 2A) were characterized by scanning electron microscopy (SEM), as well as non-intrusive, *in situ* micrometer-scale X-ray computed tomography (micro-CT). The introduction of micro-CT enables the capability of non-destructive inspection of the battery, which can be highly beneficial to characterize the devices under deformation without the need to disassemble the cells. As shown in Figure 2B, the micro-CT images show a morphology which in agreement with the SEM images of the pristine anode, cathode, cellulose separator,

Please cite this article in press as: Yin et al., High Performance Printed AgO-Zn Rechargeable Battery for Flexible Electronics, Joule (2020), https://doi.org/10.1016/j.joule.2020.11.008

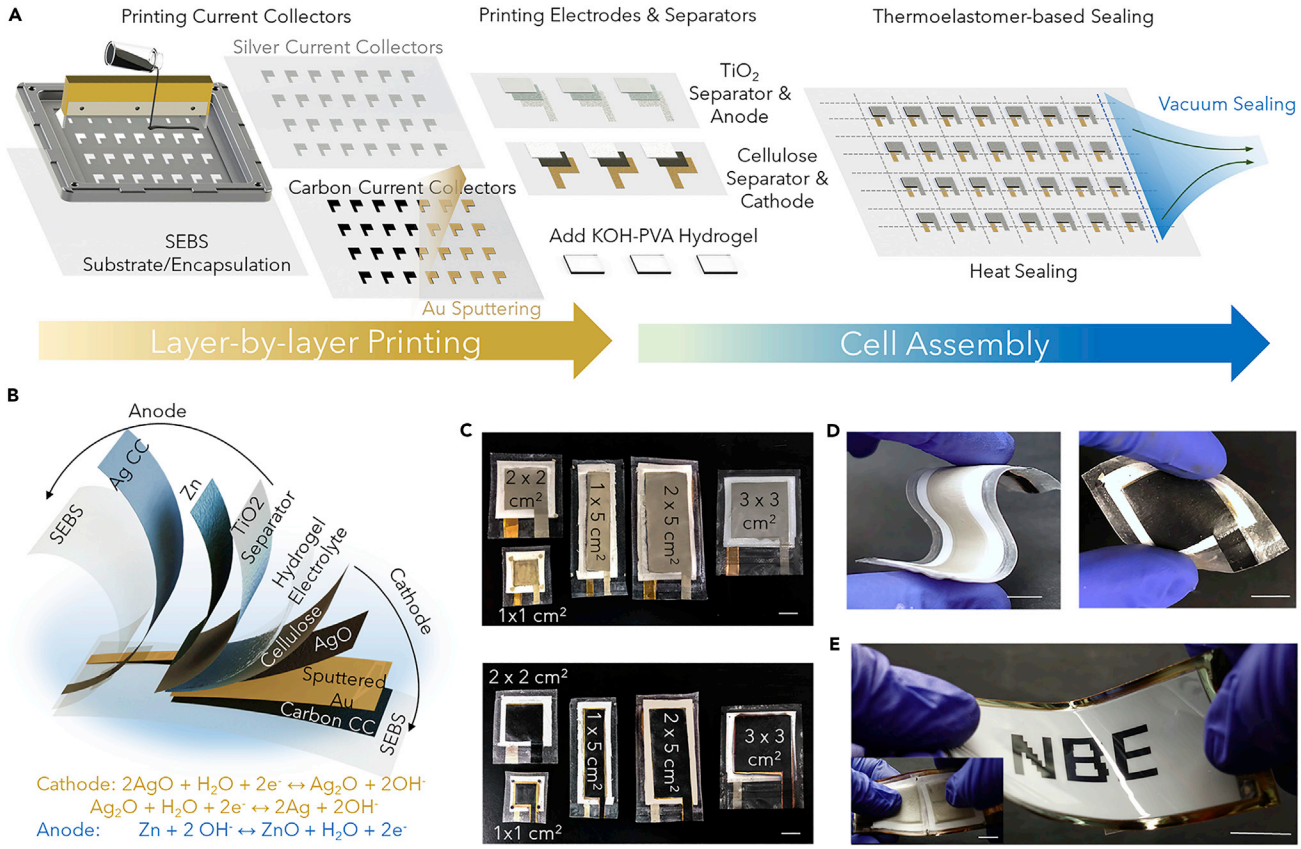

Figure 1. All-Printed Fabrication of the Flexible, Rechargeable, and High-Capacity AgO-Zn Battery

(A) Illustration of the layer-by-layer printing and vacuum-sealing assembly processes.

(B) Illustration of the AgO-Zn battery cell structure. The cell is composed of a hydrogel electrolyte sandwiched between the 2 electrodes, with each side composed of a heat-sealable SEBS substrate, current collectors, active material electrodes, and corresponding separators.

(C) Photo images of the assembled cells in different customized sizes.

(D) Photo images demonstrating the flexibility of the printed batteries.

(E) Photo images of a flexible E-ink display system powered by the flexible AgO-Zn batteries. Scale bar, 1 cm. See also Figures S2–S4.

and TiO_2 separator. Accordingly, the 3-dimensional (3D) imaging of these films shown in Figure S21 offers a more comprehensive understanding of the material structures. The loosely packed Zn anode used in this work is made of large particles, with sizes in the range of 50–100 μm, which hence reduces the surface passivation induced by the spontaneous reaction with the electrolyte. Energy dispersive X-ray analysis (EDX) further shows the homogeneous coverage of the Bi_2O_3 and the fluoropolymer binders on the surfaces of the Zn particles (Figure S5). As the dissolved zincate ion preferably redeposits on to the Bi surface during charge, this homogeneous coverage of the Bi_2O_3 particles can reduce the possible formation of Zn dendrite. The TiO_2 separator contains much smaller particles to form a dense and homogeneous film, thus can effectively reduce the dendrite growth by providing a field of nucleation sites for the dissolved zincate ions to precipitate on to next to the anode (Figure S7). In comparison, the AgO electrode uses 1–20 μm particles to produce a porous electrode, which was paired with a separator with similar particle sizes to capture the dissolved Ag species (Figures S6 and S8). Overall, with good wetting, the porous electrodes facilitate the permeation of the electrolyte, thus allowing the fabrication of cells with thicker electrodes to increase areal capacity. The conductivity of the PVA-based electrolyte (Figure 2C) is in the 10^2 mS/cm order in a wide range of temperatures (−10°C to 60°C), similar to that of other gel

Please cite this article in press as: Yin et al., High Performance Printed AgO-Zn Rechargeable Battery for Flexible Electronics, Joule (2020), https://doi.org/10.1016/j.joule.2020.11.008

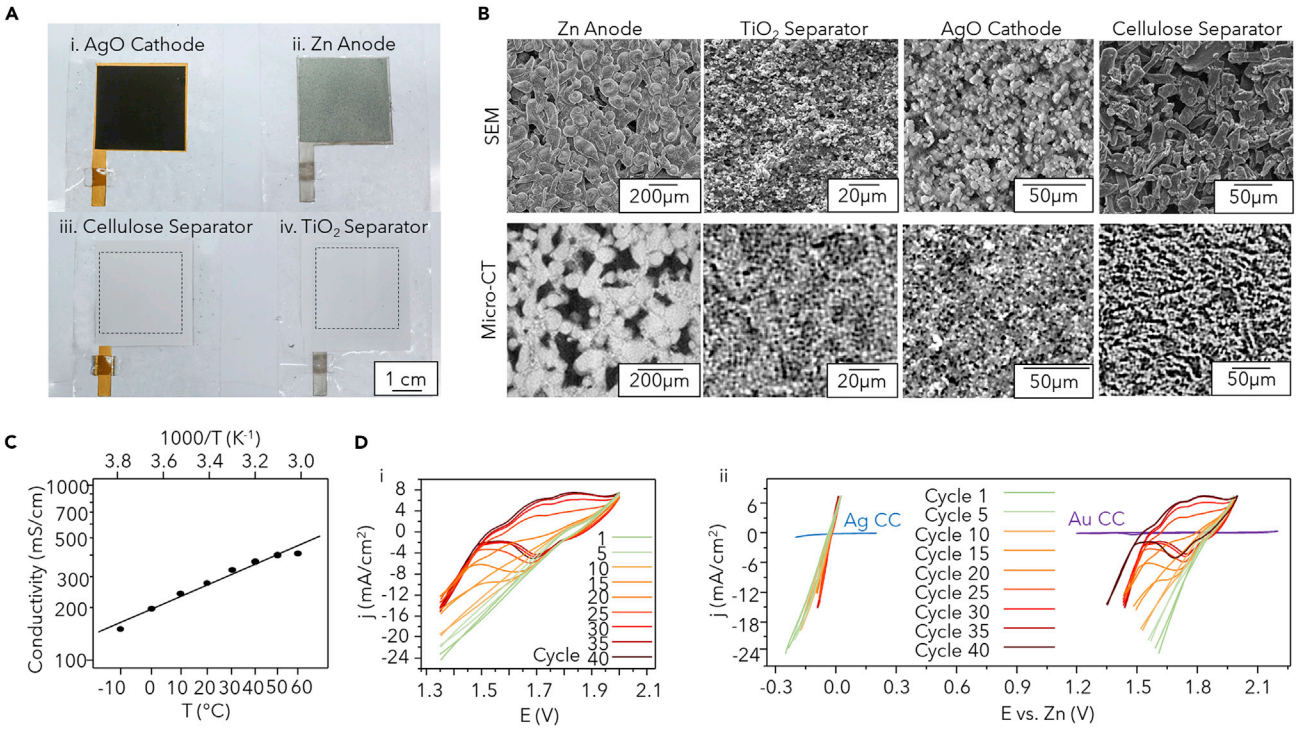

Figure 2. Morphological and Electrochemical Characterization of the Printed Battery

(A) Photo images of the printed 3 × 3 cm^2 cell with the (i) AgO electrode, (ii) Zn electrode, (iii) cellulose separator, and (iv) TiO_2 separator layers.

(B) Microscopic images of corresponding layers of the cell taken via SEM and Micro-CT.

(C) The conductivity of the gel electrolyte as a function of temperature.

(D) 40 cycles of CV between 2 and 1.35 V of the (i) full cell and (ii) corresponding potential shifts in the anode (left) and the cathode (right) using a 3-electrode cell with a Zn metal pseudo-reference electrode. The CVs of the current collectors within the corresponding voltage windows (anode −0.3–0.3 V, cathode 1.2–2.2 V) under the electrolyte environment are overlaid onto the electrode CVs. Scan rate: 10 mV/s. See also Figures S5–S11.

electrolytes reported in the literature.[15,38] The solid-phase hydrogel holds the ability to properly wet the electrodes, which allows higher current cycling, while serving as a leak-free electrolyte barrier blocking dendrite growth. The hydroxide concentration was shown to have little effect on the electrolyte conductivity (Figure S9) but had a significant impact on the cycle life of the battery (Figure S13) and was thus optimized to be 36.5% by weight.

Figure S10 displays 3-electrode cells, using a Zn foil as a pseudo-reference electrode that was used for cyclic voltammetry (CV) analysis. The AgO-Zn battery is designed to charge and discharge within the window of 1.35 to 2 V, which is used as the CV scanning range. As shown in the full cell CV in Figure 2Di, within the scanning rate of 10 mV/s, the cell can undergo a high current density of up to 20 mA/cm^2, proving the cell's ability to discharge at high current. It is worth noting that during the CV scan, the battery is being discharged, leading to a shift in the voltammogram; as the scanning proceeds, the charge current and the discharge current move toward equilibrium in the later CV cycles. Using the external Zn reference, the full cell CV can be used to gauge the potential shifts of each electrode separately. As shown in Figure 2Dii, the relative anode potential (left) does not shift significantly during the sweep, whereas the cathode potential (right) contributes to the majority of the potential change in the cell, suggesting that the AgO cathode is being the rate-limiting electrode in the charge-discharge process. The CV of the current collectors in the corresponding voltage window (Figure S11) is overlaid in Figure 2Dii,

Please cite this article in press as: Yin et al., High Performance Printed AgO-Zn Rechargeable Battery for Flexible Electronics, Joule (2020), https://doi.org/10.1016/j.joule.2020.11.008

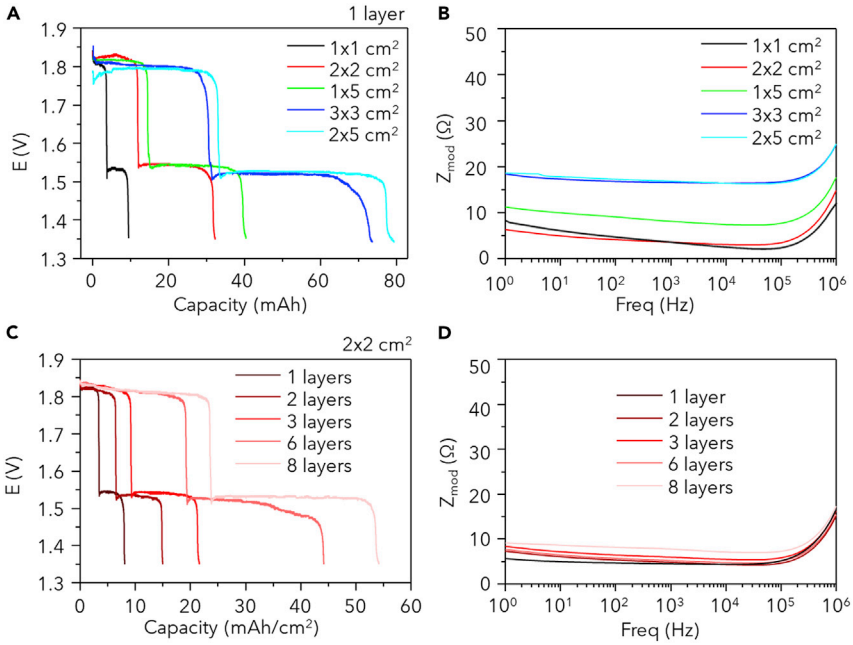

Figure 3. Electrochemical Performance of the AgO-Zn Cells as Primary Batteries

(A) The obtainable capacity of various sizes of cells that were printed with 1 layer of active materials, discharged at a current of 1 mA.

(B) Bode plot reflecting the corresponding impedance of cells of different sizes.

(C) The obtainable capacity of the 2 × 2 cm^2 cells with active material loading from 1 layer to 8 layers.

(D) Bode plot reflecting the corresponding impedance of the 2 × 2 cm^2 cells with different areal loading.

demonstrating the electrochemical stability of the current collectors within the expected potential range. It is worth noting that the current density of the Ag current collector increases toward the negative potential direction, which corresponds to the possible hydrogen evolution reaction taken place on the anode during the charging process. Such undesirable reaction is generally avoided, as lower current density is used in the normal charging processes, corresponding to lower anode polarization (Figure S18).

AgO-Zn Battery as A High Areal Capacity Primary Cell

The ability of the cell design to adapt to different cell sizes and areal loadings was evaluated. Cells with the same electrode thickness but different form factors, by varying the electrode designs, as well as the cells with the same form factors and different thicknesses by varying the number of layers of active material printed, were fabricated and discharged at a constant 1 mA current. As shown in Figure 3A, cells with 1-layer (anode ~ 120 μm, ~ 45 mg/cm^2, cathode ~ 75 μm, ~ 26 mg/cm^2) electrode thickness with the sizes of 1 × 1, 2 × 2, 1 × 5, 2 × 5, and 3 × 3 cm^2 were prepared, and the capacity increases proportionally to the cell area, with an average areal capacity of 8 mAh/cm2. Two distinct plateaus observed in the discharge voltage curves correspond to the transition of AgO to Ag_2O (~1.8 V) in the beginning of the discharge and the transition of Ag_2O to Ag (~1.5 V) as the higher-oxidation-state AgO depletes in the cathodes. The impedance of these cells was measured via 2 electrodes electrochemical impedance spectroscopy (EIS), presented in Figure 3B. The overall increase in impedance throughout the high-frequency and low-frequency domain suggests an increase in cell contact resistance,

Please cite this article in press as: Yin et al., High Performance Printed AgO-Zn Rechargeable Battery for Flexible Electronics, Joule (2020), https://doi.org/10.1016/j.joule.2020.11.008

caused by the increase in resistance of the current collector as the cell size increases. Cells with a size of 2 × 2 cm^2 were also characterized with increasing areal loadings by printing 1, 2, 3, 6, and 8 layers of electrodes. As demonstrated in Figure 3C, as the areal loading of active material increases, the areal capacity of the cell increases proportionally, reaching as high as 54 mAh/cm^2 with 8 layers of electrodes (anode ~ 800 μm, ~ 310 mg/cm^2, cathode ~500 μm, ~ 180 mg/cm^2). The EIS on the cells with different thicknesses also showed no significant impedance increase as the thickness increases: only a minor increase in impedance in the low-frequency domain suggests a slight increase in the diffusion resistance due to thicker electrodes (Figure 3D). This negligible increase can be attributed to the large pore sizes in both the anode and the cathode relative to the size of the hydroxide ions (OH^-), which applies negligible hinderance to the OH^- ion mass transfer when diffusing through the electrodes. Overall, the printed AgO-Zn cell was able to uphold superior performance in a wide range of sizes and areal loading, thus proving its customizability as a primary battery to power various electronics with appropriate sizes and capacity. A comparison between this and other flexible batteries is shown in Table S1 and Figure S1, showing the obtained areal capacity of 54 mAh/cm^2 being the highest among all printed batteries.

AgO-Zn Battery as High-Performance Secondary Cell

Beyond the application as a primary battery, the electrochemical performance of the flexible AgO-Zn battery as a secondary cell was also characterized. As a cell operating with conversion-type chemistry, it is crucial to avoid over-oxidation of the anode materials or over-reduction of the cathode materials that would lead to irreversible particle shape change. Previous studies report that the loss of capacity in this system is due to the increased thickness of the ZnO layer that passivates the anode surface, as well as the coarsening of the AgO and Ag_2O particles leading to a decrease in the cathode surface area.[8,36] Such behavior can be effectively mitigated by accurately controlling the degree of charge and discharge to limit the occurrence of irreversible electrode shape changes. The optimized charge-discharge algorithm was determined to cycle the cell between 40% and 90% of its maximum capacity, with larger ranges resulting in lower cycle life as shown in Figure S12. Figure 4A demonstrates the cycling of a cell with 2-layer electrodes with a maximum capacity of ~ 16 mAh/cm^2. First, a formation cycle is performed, discharging 10 mAh/cm^2 (60% of max. areal capacity) at the rate of 0.1 C, allowing the electrode to slowly relax into its preferred morphology with increased surface area and reduced impedance. Then, the batteries were charged at 0.2 C rate until reaching 2 V and charged at constant voltage until the C-rate dropped to below 0.04 C or the capacity reached 8 mAh/cm^2 (50% of max. areal capacity). The battery was then discharged at 0.2 C until reaching a columbic efficiency of 100% or a voltage of 1.35 V. The entire charge-discharge process is accurately controlled by capacity in the initial cycles, ensuring the cell is cycled between 40% to 90% of its maximum capacity. As shown in Figure 4C, after a few cycles at the rate of 0.2 C, the cell slowly relaxed from capacity-controlled discharge to voltage-controlled discharge, with the higher plateau to lower plateau ratio resembling the behavior of the primary cells. Using such charge-discharge algorithm, the cycle life of the unstable AgO oxidation state could be controlled, and a significantly increased cycle life can be obtained compared with previous studies.[10,29,39] Due to the supersaturation-precipitation reaction mechanism of both the anode and the cathode during discharge, the cell can be discharged at a high C-rate of up to 1 C without any loss in capacity and columbic efficiency, as shown in Figures 4A and 4B. Recharging the battery at a higher C-rate is also possible, as shown in Figure S14. However, the high C-rate would lead to an increase in the upper plateau voltage, which increases

Please cite this article in press as: Yin et al., High Performance Printed AgO-Zn Rechargeable Battery for Flexible Electronics, Joule (2020), https://doi.org/10.1016/j.joule.2020.11.008

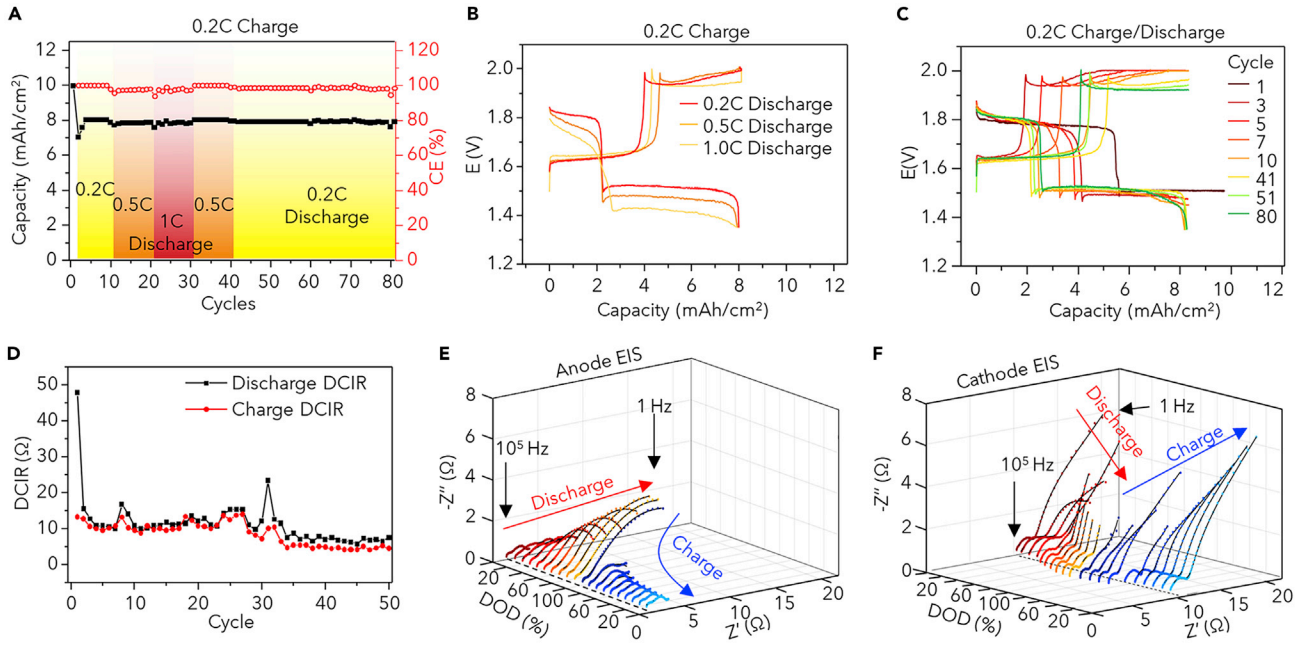

Figure 4. Electrochemical Performance of the AgO-Zn Cells Operating as Rechargeable Batteries

(A) The cycling performance of the printed battery with a charging C-rate of 0.2 C and varying discharge rates of 0.2, 0.5, and 1 C.

(B) The voltage-capacity plot of the battery under different discharging C-rates.

(C) The voltage-capacity plot of the AgO-Zn battery at different number of cycles showing the stabilization of the charge-discharge profile.

(D) The DCIR of the AgO-Zn within 50 cycles cycled at the C-rate of 0.2 C.

(E and F) The EIS profile of the (E) Zn anode and (F) AgO cathode within 1 complete discharge-charge cycle on a 3-electrode cell with a Zn metal pseudo-reference electrode. See also Figures S12–S18.

the risk of oxygen evolution on the cathode and reduces the cell rechargeability and thus was not preferred.

Impedance measurements of the flexible batteries showed relatively low impedances throughout cycling. The impedance of the batteries was either determined during cycling of the full-cell using direct current internal resistance (DCIR) method or during cycling of the separated anode and cathode half-cells using a 3-electrode configuration with a Zn foil serving as the reference. The DCIR analysis offers a straightforward and simple way to gauge the change in the internal resistance of the battery. As shown in Figure 4D, 2-electrode DCIR analysis with both charging and discharging current was performed before each charge and discharge for a battery cycling at 0.2 C, and the battery was able to maintain low internal resistance throughout the cycles, suggesting no formation of high-impedance passivating layers on the surface of the electrode throughout cycling. To obtain detailed information on the change in the impedance of each electrode during each cycle, multiple 3-electrode EIS analyses were performed on the battery while cycling at 0.2 C and were plotted against the degree of discharge (DOD) of the battery. As presented in Figure 4E, the anode half-cell started at a low impedance of 1–4 Ω, with 2 depressed semicircles attributed to the high-speed charge transfer at the Zn particle interface and the lower speed hydroxide ions (OH^-) diffusion in the porous network.[38] With discharging, the low-frequency semicircle slowly expands due to the formation and growth of the ZnO species that impedes the OH^- transport and increases the double-layer capacitance. During charging, the oxygen species are liberated from the reactions in Equations 1, 2, and 3 to form OH^- ions that diffuse readily out of the anode. This results in the fast mass transport of OH^- ions out of the

Please cite this article in press as: Yin et al., High Performance Printed AgO-Zn Rechargeable Battery for Flexible Electronics, Joule (2020), https://doi.org/10.1016/j.joule.2020.11.008

anode and a rapid drop in the impedance at the onset of charging that eventually recovers to the initial level, thus showing the reversibility of the anode. For the cathode half-cell EIS shown in Figure 4F, at the start of the discharge (0% DOD), a single semicircle corresponding to the mass transfer resistance and capacitance of the Ag_2O formation is observed with a low-frequency impedance tail at an angle of approximately 45°, suggesting standard Warburg diffusion of OH^-. As the cell is discharged, the overall impedance decreases with a second semicircle emerging near the low-frequency domain that can be attributed to the charge transfer resistance and capacitance of Ag formation from Ag_2O. During charging, this second low-frequency semicircle disappears, as all the Ag oxidizes to form Ag_2O and eventually AgO.

Overall, the 3-electrode impedance results provide a deeper insight into the reaction and possible routes in improving the battery's cycle life and performance. These data indicate that the impedance of the AgO cathode is responsible for the majority of the cell impedance. Therefore, a beneficial next step will be to incorporate additives that can increase the cathode electrical conductivity to improve the performance in high-current applications. For the anode, the monitoring of ZnO formation via EIS can be paired with topological characterization methods to better control the conversion of Zn electrodes toward extended cycle life and is expected to be extremely useful for future analysis. More data and discussion of 3-electrode EIS can be found in the supplementary section and Figures S15–S17.

Mechanical Stability of the Flexible AgO-Zn Battery

Compared to coin cells, cylindrical, or prismatic cells, the printed flexible batteries have the unique advantage of allowing bending, flexing, and twisting without causing sudden structural failure. To endow such mechanical resiliency, the printed AgO-Zn batteries are composed of flexible and stretchable polymer-particle composite layers containing highly elastic binders that can accommodate for the applied strain while maintaining the overall structural integrity. During bending, this flexibility and stretchability allows the layers to elongate on the outer rim of the arc to react to the tensile strain, thus allowing the battery to avoid delamination between layers even when very thick electrodes are used. After vacuum sealing, the atmospheric pressure is exerted to the cell and intimate contact is ensured between the different layers, further avoiding possible delamination. To test the performance of the batteries under small-radius, large-angle deformation, a 2-layer 1 × 5 cm^2 cell was fabricated and discharged at a current of 1 mA while undergoing repeated bending and twisting deformations. As illustrated in Figures 5A and 5B, the cell was tested manually with 180° and 360° bending toward anode (outward) and toward cathode (inward) around a cylinder with a radius of 0.5 cm, as well as 180° twisted in both directions from head to end. The corresponding voltage change during 100 cycles (1 s per cycle) of deformation was recorded, as shown in Figure 5C. In general, the cell exhibited stable performance during bending and twisting in both directions, with negligible fluctuation in voltage during the 180° bending cycles and roughly 10 mV fluctuation during the 180° bending and twisting cycles. The inward bending in general shows slightly more variations, which is suspected to be caused by the softer Ag current collector on the anode size undergoing more stretching on the outside during bending. More data of the cell under 10% stretching deformation can be found in Figure S20. The effect of bending to the capacity of the cell was also analyzed via a small-radius repeated bending experiment. A 1 × 5 cm^2 battery was first bent inward 360° for 500 times with a bending radius of 0.5 cm and was then charged and discharged for 10 cycles. Thereafter, the battery was similarly bent outward 360° for 500 times and charged and discharged for 10 more cycles. As shown on Figure 5D, no significant drop in capacity nor coulombic efficiency was observed after the bending cycles, hence demonstrating the stable mechanical

Please cite this article in press as: Yin et al., High Performance Printed AgO-Zn Rechargeable Battery for Flexible Electronics, Joule (2020), https://doi.org/10.1016/j.joule.2020.11.008

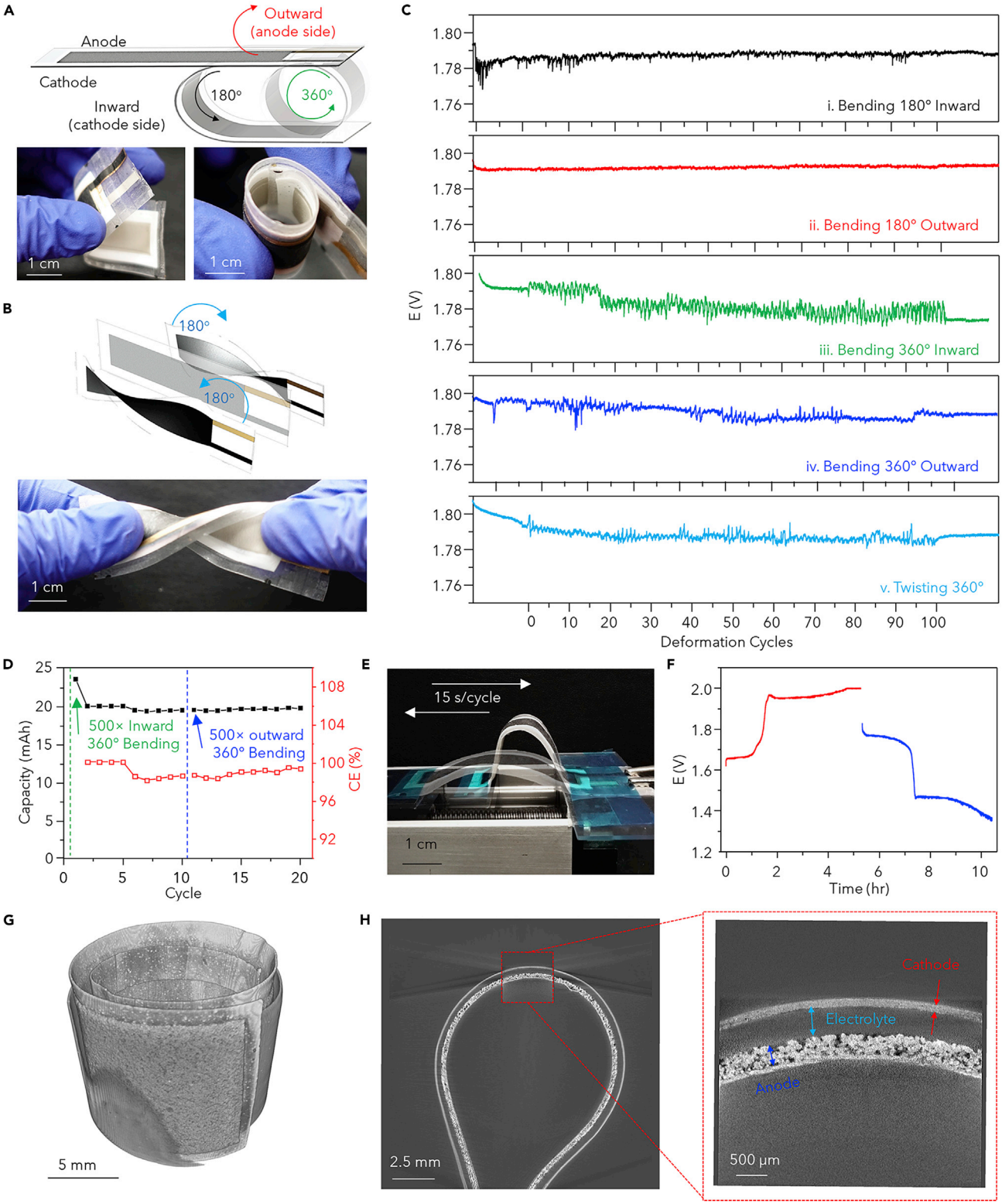

Figure 5. Performance of the AgO-Zn Cell under Various Mechanical Deformations

(A and B) (A) Illustrations and corresponding photo images of a 2-layer loading, 1 × 5 cm^2 battery undergoing (A) 180° and 360° bending deformations and (B) 360° twisting deformation.

Please cite this article in press as: Yin et al., High Performance Printed AgO-Zn Rechargeable Battery for Flexible Electronics, Joule (2020), https://doi.org/10.1016/j.joule.2020.11.008

Figure 5. *Continued*

(C) The corresponding voltage profile of the battery during 1 mA discharge while undergoing 100 cycles of (i) 180° outward bending, (ii) 180° inward bending, (iii) 360° inward bending, (iv) 360° outward bending with a bending diameter of 1 cm, and (v) 360° head-to-end twisting.

(D) Assessing the effect of bending to the capacity of the battery. A 2-layer loading, 1 × 5 cm^2 battery undergoing 500 cycles of inward 360° bending and 500 cycles of similar 500 cycles of outward bending demonstrated no drop in battery capacity nor coulombic efficiency.

(E and F) (E) Photo illustration of a battery under repeated 180° bending cycles controlled by a linear stage at the speed of 15 s/cycle and (F) the corresponding voltage-time plot of the charging (red) and discharging (blue) of the battery during ~2,500 repetitions of bending.

(G and H) (G) The micro-CT image of the entire 1 × 5 cm^2 cell after repeated bending and twisting cycles rolled in a diameter of 1 cm and (H) the cross-section of it bent in a diameter of 1 cm (left) and a zoomed-in view (right) of the electrodes, demonstrating no structural damage or delamination of the cell after repeated mechanical deformations. See also Figures S19–S21.

performance of the battery as a flexible, rechargeable cell. The rechargeability of the cell was also not interrupted by the repeated deformation during cycling, as shown in Figures 5E and 5F; Video S1, where the battery can be normally charged and discharged while undergoing ~2,500 cycles of 180° bending cycles. To ensure the mechanical stability of the cell, micro-CT was used to characterize the cell after the repeated deformation. As shown in Figures 5G and 5H, the entire cell can be scanned at a high resolution to obtain a 3-dimensional (3D) image reflecting the microscopic structure of the cell under deformation after repeated bending and twisting. The zoom-in view of the cross-section of the battery further shows no cracks or delamination after the repeated bending cycles, reflecting the robust mechanical resiliency of the battery against such deformation. More 3D visualizations of the battery under bending deformation can be found in Figure S21. Overall, pairing the superior electrochemical and mechanical performance, the printed AgO-Zn battery is proven to be well-suited to reliably and sustainably power various wearable and flexible electronics.

Powering Flexible Electronics

To demonstrate the performance of the battery powering typical flexible electronics, we designed a flexible E-ink display system controlled by an Arduino-type microcontroller unit with added Bluetooth communication module, which resembles many prototypes of IoT, wearable, and flexible devices (Figures 6A and S22). The system is powered by two 2 × 2 cm^2 batteries with 2-layer electrodes connected in series, which can supply enough voltage (>3 V) to boot the system. A mobile device can connect and transmit data and commands to the BT module, which is processed by the microcontroller that refreshes the E-ink display. First, the energy consumption of the system under different operation modes operating at 3.6 V was measured. Figure 6B displays the current draw when (1) the system is broadcasting to seek for connection, which contains short bursts of current peaks around 20 mA (in black); (2) the system is connected to a mobile device, with an average current of 9 mA (in red); and (3) the system is actively transmitting data between the cellphone and the display, with the current alternating between a higher baseline of 8.5 mA with peaks of 13 mA and a lower baseline of 4 mA with peaks of 10 mA (in blue). The batteries are thus discharged using a script simulating the power consumption of the flexible E-ink display system working in repeated discrete sessions, with 10 s of BT broadcasting, 10 s of idle after establishing the connection, 10 s of active data transmission, followed by 30 s of resting (powered off) (Figures 6C and S24). As illustrated in Figure 6D, The 2 batteries in series were able to sustain the pulsed, high-current discharge in the 3.6–2.4 V window to deliver power to the system constantly for over 12 h and were able to maintain their capacity of ~60 mAh, similar to the capacity obtained from the constant low-current 1 mA discharge. By pairing with the high-areal capacity flexible AgO-Zn battery, the flexible E-ink display was able to operate while undergoing bending deformations, which is demonstrated in Video S2. In comparison, commercial Li coin cells with similar rated capacity were not able to sustain the high current pulsed discharge, resulting in a significant loss in capacity when

Please cite this article in press as: Yin et al., High Performance Printed AgO-Zn Rechargeable Battery for Flexible Electronics, Joule (2020), https://doi.org/10.1016/j.joule.2020.11.008

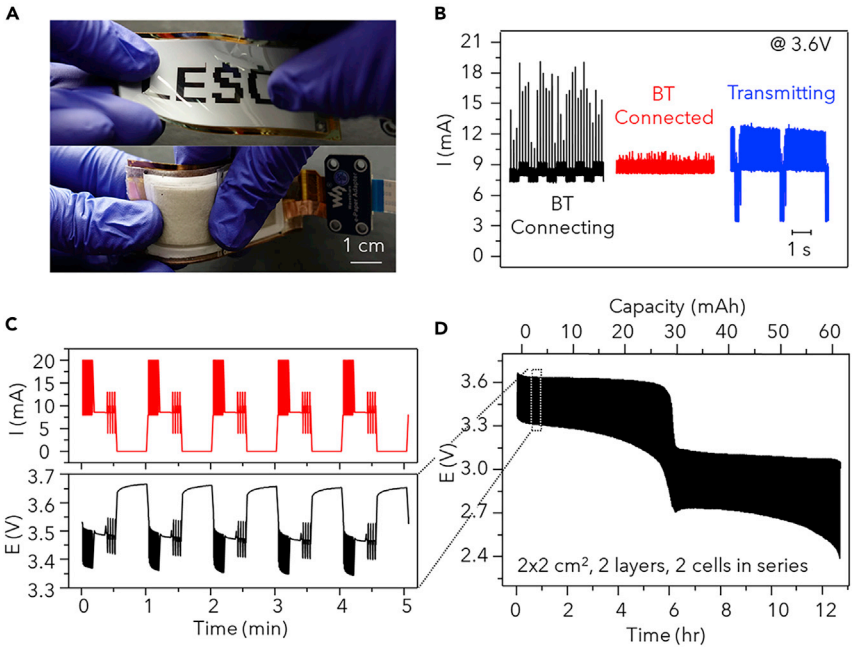

Figure 6. The Powering of a Flexible E-Ink Display System by the Flexible AgO-Zn Batteries

(A) Photo images of the flexible E-ink display and the placement of two 2-layer loading, 2 × 2 cm^2 batteries connected in series on the back of the display.

(B) The power consumption of the E-ink display system with integrated BT and MCU modules during BT connection (black), after establishing the connection (red), and during active data transmission (blue).

(C) Simulated discharge current profile with varying pulses and baselines (red) and the corresponding voltage response of the battery (black).

(D) The complete discharge profile of the 2 cells connected in series implementing the simulation discharge profile. See also Figures S22–S25.

discharged using the same script (Figure S24). The low-impedance and high-energy-density battery is therefore proven to have both outstanding electrochemical and mechanical performance for powering of a typical prototype of a flexible electronic system. With performances even surpassing non-flexible commercial coin cells counterpart, this all-printed battery can be considered extremely attractive owing to its customizability and flexibility toward real-life applications. A typical application of using this battery to illuminate an LED bulb while applying various mechanical deformations was also tested, where the light intensity did not change as the battery was bent, folded, twisted, and stretched (Video S3).

DISCUSSION

In this work, we have demonstrated a flexible and high-performance AgO-Zn battery based on the rechargeable conversion chemistry. Using specially formulated ink with stretchable elastomeric binders and thermoplastic elastomeric substrates, the batteries can be printed layer-by-layer using low-cost, high-throughput screen-printing techniques and assembled with heat- and vacuum-sealing processes. To obtain a low device footprint while maintaining easy processability, printable and flexible separators and a solid-phase KOH-PVA hydrogel were developed to allow a stacked sandwich configuration. The printable battery is compatible with various cell sizes and areal loading, leading to a high areal capacity of 54 mAh/cm^2 in connection to repeated multilayer printing for primary applications. The battery is also rechargeable upon implementing the capacity-controlled cycling algorithm, with high cycle

Please cite this article in press as: Yin et al., High Performance Printed AgO-Zn Rechargeable Battery for Flexible Electronics, Joule (2020), https://doi.org/10.1016/j.joule.2020.11.008

life beyond 70 cycles with varying discharge C-rates without loss in capacity and coulombic efficiency. The battery exhibited low impedance within each discharge-charge cycle while maintaining low internal resistance throughout multiple cycles, suggesting a stable and reversible electrode morphological change during electrode redox reactions. As a flexible energy storage unit for powering various flexible, wearable electronics, the performance of the battery was evaluated under rigorous mechanical testing, demonstrating that the battery offers remarkable resiliency against repeated large deformation bending and twisting cycles. The fabricated batteries were used in the powering of a customized flexible E-ink display system with BT connectivity and delivered an outstanding performance that surpassed commercial coin cells under the high-current pulsed discharge regime required by the electronics. Future work leveraging advanced electrochemical and topological characterization on this promising battery chemistry will be conducted to further improve its performance and cycle life. This will involve further optimization of the fabrication process, the ink composition, and the layer thicknesses and porosities should lead to a practical, commercially viable product with higher cycle life, lower impedance, smaller device footprint, and lower production cost. Overall, this work demonstrates the scalable fabrication of flexible AgO-Zn batteries with highly desirable electrochemical and mechanical performance and tremendous implications toward the development of novel energy storage devices for the powering of next-generation electronics.

EXPERIMENTAL PROCEDURES

Resource Availability

Lead Contact

Further information and requests for resources and materials should be directed to and will be fulfilled by the Lead Contact, Ying Shirley Meng (shmeng@ucsd.edu).

Material Availability

This study did not generate new unique materials.

Data and Code Availability

The data of this study are available from the authors upon reasonable request.

Chemicals

Bi_2O_3, $Ca(OH)_2$, KOH (pellets, ≥85%), LiOH, 4-methylpentan-2-one (MIBK), toluene, cellulose (microcrystalline powder, 20 μm), Triton-X 114, Poly(ethylene oxide) (PEO) (MW 600,000), and PVA (MW = 89,000 – 98,000, 99+% Hydrolyzed) were purchased from Sigma Aldrich (St. Louis, MO, USA). Zn (Grillo-Werke AG, Germany), AgO (Ames Goldsmith, South Glens Falls, NY, USA), and TiO_2 (CR-470, Tronox Holdings plc, New York, NY, USA) were obtained from ZPower LLC (Camarillo, CA, USA). The fluorocopolymer (GBR-6005, poly(vinylfluoride-co-2,3,3,3-tetrafluoropropylene)) was obtained from Daikin US Corporation (New York, NY, USA). SEBS (G1645) was obtained from Kraton (Houston, TX, USA). Graphite powder was purchased from Acros Organics (USA). Super-P carbon black was purchased from MTI Corporation (Richmond, CA, USA). All reagents were used without further purification.

Cell Fabrication

Formulation of the Flexible Inks

The electrode resin was prepared by adding 5 g of the fluorine rubber in 10 g of MIBK solvent and left on a shake table overnight, until the mixture was

Please cite this article in press as: Yin et al., High Performance Printed AgO-Zn Rechargeable Battery for Flexible Electronics, Joule (2020), https://doi.org/10.1016/j.joule.2020.11.008

homogeneous. The SEBS resin was prepared by adding 40 g of the SEBS into 100 mL of toluene and left on a shake table until the mixture was homogeneous.

The silver current collector ink was formulated by combining Ag flakes, SEBS resin, and toluene in 4:2:1 weight ratio and mixing in a planetary mixer (Flaktak Speedmixer™ DAC 150.1 FV) at 1,800 rotations per minute (rpm) for 5 min.[40] The carbon current collector ink was formulated by firstly mixing graphite, Super-P, and PTFE powder in 84:14:2 weight ratio with a set of pestle and mortar. The mixed powder was mixed with the SEBS resin and toluene in a 10:12:3 weight ratio using the mixer at 2,250 rpm for 10 min to obtain a printable ink.[10]

The Zn anode ink was formulated by firstly mixing the Zn and Bi_2O_3 powders in a 9:1 weight ratio with a set of pestle and mortar until the Zn particles are evenly coated with the Bi_2O_3 powder. The evenly mixed powder was then mixed with the electrode resin and MIBK in a 20:4:1 weight ratio using the mixer at 1,800 rpm for 5 min to obtain a printable ink. The AgO cathode ink was formulated by firstly mixing the AgO and Super-P powders in a 95:5 weight ratio using a set of pestle and mortar until homogeneous. The powder was then mixed with the electrode resin and MIBK in 5:5:2 weight ratio using the mixer at 2,250 rpm for 5 min to obtain a printable ink.

The TiO_2 separator ink was prepared by firstly mixing TiO_2 and cellulose powder in a 2:1 weight ratio using a set of pestle and mortar. The mixed powder was then added with the SEBS resin, toluene and Triton-X in 50:55:75:3 weight ratio and mixed with the mixer at 2,250 rpm for 10 min to obtain a printable ink. The addition of Triton-X surfactant in the anode separator ensures the proper wetting of the thick Zn anode, hence increase the effective electrochemical surface area of the anode and avoid high local current density that would lead to dendrite growth. The cellulose separator ink was prepared by firstly mixing TiO_2 and cellulose powder in a 26:9 weight ratio using a set of pestle and mortar. The mixed powder was then added with the electrode resin, MIBK in an 8:7:4 weight ratio and mixed with the mixer at 2,250 rpm for 10 min to obtain a printable ink.

All inks above were formulated empirically to obtain a screen-printable consistency, which was adjusted with various amounts of solvent to achieve good printing quality. The particle size distribution of the powders used in this work is summarized in Table S3.

Preparation of The SEBS Substrate

SEBS was dissolved in toluene with a weight ratio of 6 to 8.7 and was left on a linear shaker (Scilogex, SK-L180-E) overnight or until the mixture became transparent and homogeneous. Wax paper was used as the temporary casting substrate, and a film caster with the clearance of 1,000 um was used to cast the SEBS resin onto the wax paper. The cast resin was firstly dried in the ambient environment for 1 h, followed by curing in a conventional oven at 80°C for 1 h to remove the excess solvent. The transparent, uniform SEBS film, which can be readily peeled off from the wax paper after curing, was used as the substrate for subsequent battery printing.

Printing of the Electrodes

Stencils for printing the current collectors, electrodes, and separators were designed using AutoCAD software (Autodesk, San Rafael, CA, USA) and produced by Metal Etch Services (San Marcos, CA), with dimensions of 12 in × 12 in. The stencils used in this work were stainless steel cut-out stencils without meshes. The thickness of the stencils was designed to be 100 μm for the carbon and silver current collectors,

Please cite this article in press as: Yin et al., High Performance Printed AgO-Zn Rechargeable Battery for Flexible Electronics, Joule (2020), https://doi.org/10.1016/j.joule.2020.11.008

300 μm for the TiO_2 separator and the Zn anode, and 500 μm for the cellulose separator and the AgO cathode. The printing of the following layers was performed using a semi-automatic MPM-SPM printer (Speedline Technologies, Franklin, MA, USA) with an 8-in metal blade squeegee. The stencil and squeegee pressure were optimized for each stencil, correspondingly. To print the anode, the silver ink was first printed onto the SEBS substrate and cured in a conventional oven at 80°C for 10 min. The Zn ink was then printed onto the silver current collectors and cured at 80°C for 30 min. The TiO_2 ink was lastly printed onto the anode and cured at 80°C for 10 min. To print the cathode, the carbon ink was firstly printed onto the SEBS substrate and cured at 80°C for 10 min. polyethylene terephthalate (PET) sheets were cut using a computer-controlled cutting machine (Cricut Maker®, Cricut, Inc., South Jordan, UT, USA) into a mask exposing the printed carbon electrodes, and the masked carbon current collector was sputtered with ~ 400 nm of Au and adhesion interlayer of Cr at a DC power of 100 and 200 W respectively and an Ar gas flow rate of 16 SCCM using a Denton Discovery 635 Sputter System (Denton Discovery 635 Sputter System, Denton Vacuum, LLC, Moorestown, NJ, USA). The AgO ink was then printed onto the sputtered current collectors and cured at 50°C for 60 min. Lastly, the cellulose ink was printed onto the cathode and cured at 50°C for 60 min. To print multiple layers of electrodes or the separators, the stencil was offset by an additional 65 μm for each layer of AgO and 100 μm for each layer of Zn to compensate for the electrode thickness. See Figure S2 for the step-by-step printing and assembly process of the batteries and Figure S3 for the thickness calibration for the printing of anode and cathode.

Synthesis of the Electrolyte Hydrogel

The hydrogel is synthesized by mixing the PVA solution and the hydroxide solution into a gel precursor and dried in a desiccator until the desired weight is reached. For synthesizing the 36.5% hydroxide gel used in this study, the following formulations were used. A hydroxide solution was prepared by dissolving 9.426 g KOH and 0.342 g LiOH into 50 mL deionized (DI) water. 0.5 g $Ca(OH)_2$ was then added into the solution and stirred in a closed container under room temperature for 1 h to saturate the solution with $Ca(OH)_2$, and the excess $Ca(OH)_2$ was then removed from the solution. A PVA solution was prepared by dissolving 4.033 g PVA and 0.056 g PEO into 50 mL DI water heated to 90°C. The precursor solution was prepared by mixing the hydroxide solution and the PVA solution in the weight ratio of 13.677:10 and poured into a flat petri dish with a weight of 0.2 g/cm^2. The precursor was left to dry in a vacuum desiccator until the weight decreased to 26.12% of precursor weight to obtain a soft, translucent hydrogel with its caustic material taking 36.5% of the sum of caustic material and the water content. Additional weight and conductivity information for different hydroxide concentrations can be found in Table S2. The hydrogel can be then cut into desired sizes and directly used or stored in a hydroxide solution with the same weight ratio of hydroxide without PVA. The storage solution for the 36.5% KOH-PVA gel was prepared similar to the hydroxide solution, where 10.777 g KOH, 0.391 g LiOH, and 0.5 g $Ca(OH)_2$ were dissolved into 15 mL DI water and the excess $Ca(OH)_2$ was removed. More images of the fabrication of the hydrogel are shown in Figure S4.

Microstructural Characterization

Morphological analyses of the current collectors, separators, and active material electrodes were performed with SEM and micro-CT. SEM images were taken using an FEI Quanta FEG 250 instrument with an electron beam energy of 15 keV, a spot size of 3, and a dwell time of 10 μs. Micro-CT experiments were conducted using a ZEISS Xradia 510 Versa. For individual film analysis, micro-CT samples were

Please cite this article in press as: Yin et al., High Performance Printed AgO-Zn Rechargeable Battery for Flexible Electronics, Joule (2020), https://doi.org/10.1016/j.joule.2020.11.008

prepared by punching 2 mm radii disks and stacking them in a PTFE cylindrical tube with alternating PTFE films to provide separation between neighboring film disks. For the Micro-CT of full and sealed cell bending, a 1 × 5 cm^2 AgO-Zn battery was bent or rolled around a polyethylene (PE) cylindrical tube with a diameter of 1 cm.

For the micro-CT active material electrodes, the heavier metals, such as Zn and Ag, warranted higher X-Ray energies than the printed polymer separator films. Accordingly, scans at 140 keV and a current of 71.26 μA were performed with high energy filters and a magnification of 4× on the Zn and AgO films with voxel sizes of 2.5 and 0.75 μm and exposure times of 2 and 18 s respectively. For the polymer separators, 80 keV scans with an 87.63 μA current were used with low energy filters at a magnification of 4× with voxel resolutions of 0.75 and 1.1 μm and exposure times of 8 and 1 s for the printed anode and cathode separators respectively. For scans of the full cell bending, a voltage of 140 keV and a current of 71.26 μA with a 4× magnification was performed with the following voxel resolutions and exposure times for the respective cases: 18.35 μm and 2 s for low resolution bending scan, 3.54 μm and 5 s for higher resolution bending scan, and 7.55 μm and 2 s for rolled cell scan. For all micro-CT scans conducted, 1,801 projections were taken for a full 360° rotation with beam hardening and center shift constants implemented during the data reconstruction. Post measurement imaging and analysis were performed by Amira-Avizo using the Despeckle, Deblur, Median Filter, Non-local Means Filter, Unsharp Mask, and Delineate modules for data sharpening and filtration provided by the software. The animated micro-CT scan of the battery can be found in Videos S4 and S5.

Electrochemical Characterization

Cyclic Voltammetry

The 3-electrode half-cell CV characterization was performed on a cell assembled with the printed electrodes as the working electrode, a platinum foil as the counter electrode, Zn metal foil as the reference electrode, and 2 pieces of KOH-PVA hydrogel as the electrolyte. The 3-electrode full-cell CV characterization was performed between 1.35 to 2 V on a cell assembled similar to the typical battery architecture but with an extra Zn metal foil as the reference electrode. The structures of both cells are illustrated in Figure S10. The CV was performed using an Autolab PGSTAT128N potentiostat-galvanostat with an additional pX-1000 module. In the 3-electrode full-cell CV, the AgO cathode was connected to the working electrode probe, the Zn anode was connected to the counter and reference electrode probes and the pX-1000 module was used to monitor the potential between the cathode and the reference Zn foil. The potential of the anode versus Zn was obtained by subtracting the cathode versus Zn potential from the full cell potential. A scan rate of 10 mV/s was used for all CV tests.

Discharging and Cycling Protocol

The constant current complete discharge of the battery for primary applications was performed with the following procedure. Firstly, the assembled and vacuum-sealed battery was left idle for 1 h to allow the electrolyte to fully permeate through the electrodes. Then, the battery was discharged using a battery test system (Landt Instruments CT2001A) at the desired current, until reaching the lower cut-off voltage of 1.35 V.

To enable the secondary application of the battery, cycling protocols were established that rely on the accurate control of the potential and DOD of the battery. To perform charge-discharge cycling on a fabricated battery, 50% of its maximum

Please cite this article in press as: Yin et al., High Performance Printed AgO-Zn Rechargeable Battery for Flexible Electronics, Joule (2020), https://doi.org/10.1016/j.joule.2020.11.008

capacity, which was estimated by the low-current complete discharges, was first determined as the cyclable capacity and the basis to determine C-rates of the protocol. The battery was firstly discharged at the C-rate of 0.1 C from 100% to 40% DOD. Then, the battery was recharged at the C-rate of 0.2 C until reaching 2 V, and then at 2 V until reaching 90% DOD or C-rate of 0.05 C. The battery could be then discharged and recharged at the desired C-rates between 1.35 and 2 V, with the DOD maintained between 40% and 90% of its maximum value. Unless specified otherwise, all cycling data were performed using cells with 1 × 1 cm^2 form factor with 2 layers of active electrode materials. More cycling data for two cells with 8-layer electrode thickness connected in series is shown in Figure S15.

The pulsed discharge protocol was designed to simulate the battery's performance in powering a typical MCU-controlled wearable device with integrated BT functionality. The battery was discharged using an Autolab PGSTAT128N potentiostat-galvanostat implementing fast chrono methods. See Figure S25 for the detailed discharging script.

Electrochemical Impedance Spectroscopy

EIS measurements were performed with a Biologic SP-150 in a 3-electrode configuration. The AgO-Zn three electrodes cell was fabricated with a Zn reference wire placed between an extra layer of hydrogel electrolyte and the original electrolyte layer shown in Figure 2B. The Zn reference wire was then connected to an Au sputtered heat-sealable SEBS-based printed carbon tab that was vacuum sealed to ensure complete cell sealing to hinder electrolyte dehydration. The working electrode (WE) and counter electrode (CE) were connected to the AgO cathode and Zn anode, respectively.

The impedances of the two half cells and the full cell were monitored *in situ* during charging and discharging to analyze impedance changes most closely related to practical cycling conditions with a galvanostatic-EIS (GEIS) measurement. Accordingly, the DC base current was set to the current of the charging/discharging step, while the AC amplitude was set to 300 μA, approximately one-fifth of the cycling current. The frequency sweep was between 1 MHz and 1 Hz with 10 points per decade and an average of 8 measures per frequency. The cycling script implemented with GEIS is similar to that of the capacity-limited electrochemical cycling protocol, with the exception that the voltage limits applied were 1.95 and 1.4 V versus the reference instead of the anode for the charging and discharging respectfully. For each charge and discharge step, 10 GEIS was measured for 15 complete cycles, resulting in a total of 870 separate Nyquist plots (29 steps × 10 measures × 3 cell configurations). For analysis simplicity, only the 5^{th} cycle's discharge and charge were analyzed.

Both half-cell Nyquist plots for the 5^{th} cycle's discharge and charge steps were fitted to equivalent circuits using a slightly modified version of the Zfit function available as open-source code from Mathworks.[41] Zfit utilizes another Mathworks open source code, fminsearchbnd, to minimize the error of simulated impedances with the experimental values by altering the impedance parameters (i.e., resistance values, constant phase element values, etc.) under realistic parameter boundary conditions.[42] The use of this code allowed for streamline fitting of many successive Nyquist to provide insights in observable trends in the fitted parameters. Additional data of the EIS measurement can be found in Figures S16–S18.

Electrolyte Conductivity Measurement

The ionic conductivity of the gel electrolyte was measured by a customized two-electrode (Stainless Steel 316L) conductivity cell with an inner impedance at 0.54 Ω. The

Please cite this article in press as: Yin et al., High Performance Printed AgO-Zn Rechargeable Battery for Flexible Electronics, Joule (2020), https://doi.org/10.1016/j.joule.2020.11.008

cell constant is frequently calibrated by using OAKTON standard conductivity solutions at 0.447, 1.5, 15, and 80 $mS \cdot cm^{-1}$ respectively. A constant thickness spacer was positioned between the 2 electrodes which ensure no distance changes during multiple-time measurements. The electrolytic conductivity value was obtained with a floating AC signal at a frequency determined by the phase angle minima given by EIS using the following equation: $\sigma = KR^{-Q}$, where R is the tested impedance (Ω), K is the cell constant (cm^{-1}) and Q is the fitting parameter.[43] All of the data acquisition and output were done by LabView Software, which was also used to control an ESPEC BTX-475 programming temperature chamber to maintain the cell at a set temperature in 30 min intervals.

Mechanical Deformation Tests

The mechanical testing of the battery was performed on the $1 \times 5\ cm^2$ batteries and was composed of three parts. The first part consisting of the bending and twisting of the cell with controlled bending radius and angles. For the bending tests, the sample was bent around an Eppendorf tube toward the anode (outward) or toward the cathode (inward) with a radius of 0.5 cm, until folded in half (180°) or looped around (360°), at a speed of 1 bending per second. Due to the large deformation with complex movement involved in this test, the bending of the test was conductive manually with the guidance of the tube. Similarly, the twisting of the cell was performed manually, where the $1 \times 5\ cm^2$ sample was twisted 180° clockwise followed by counterclockwise around its long axis at a speed of 1 twisting per second (Figures 5A–5C). See Figure S19 for the bending control of the battery mechanical tests. Secondly, to quantitatively assess the influence of the bending on the capacity and cycle life of the battery, 500 repetitions of 360°, 0.5 cm radius bending was applied to the sample prior to cycling the battery. The battery was then charged and discharged for 10 cycles at a rate of 0.2 C, followed by bending the battery 500 times outward 360° with 0.5 cm radius and cycled for 10 more cycles at the same rate. The capacity of the battery was monitored to quantitatively measure the influence of bending on the cell (Figure 5D). The third part of the testing was performed using a linear motor, where the $1 \times 5\ cm^2$ sample was bent freely without angle confinement, from a radius of 3 cm at 40° to the radius of 0.5 cm at 70° repeatedly, while being charged and discharged at 0.2 C (Figures 5E and 5F).

Assembly of Flexible Display Electronics

To demonstrate the battery's ability to power flexible electronics, a Waveshare 2.9-inch e-Paper flexible display was powered by two AgO-Zn batteries in series. The display module was connected to an Adafruit Feather nRF52 Bluefruit Low Energy (LE) chip and programmed using Arduino and C. The picture of the assembled system is shown in Figure S23. MATLAB code was used to convert images to hexadecimal format to be uploaded to the board and the display. The BluefruitConnect IOS app was used to connect the Adafruit chip via Bluetooth to change the display. The system diagram of the E-ink display system is shown in Figure S22. The pulsed current profile needed to power the Bluetooth chip and display was determined using an oscilloscope by measuring the voltage across a 10 Ω resistor connected in series with the circuitry. A model pulsed profile was then extracted to be applied to flexible batteries for further testing.

SUPPLEMENTAL INFORMATION

Supplemental Information can be found online at https://doi.org/10.1016/j.joule.2020.11.008.

ACKNOWLEDGMENTS

This work was supported by funding from ZPower LLC, United States and Qualcomm, United States. This work was performed in part at the San Diego Nanotechnology Infrastructure (SDNI) of UCSD, NANO3, a member of the National Nanotechnology Coordinated Infrastructure, which is supported by the National Science Foundation, United States (grant ECCS-1542148). The authors would also like to acknowledge the National Center for Microscopy and Imaging Research (NCMIR), United States. Technologies and instrumentation are supported by grant R24GM137200 from the National Institute of General Medical Sciences, United States. AgO, Zn, and TiO_2 used in this work were provided by ZPower LLC. SEBS used in this work was provided by Kraton, United States.

AUTHOR CONTRIBUTIONS

Conceptualization, L.Y., J.S., J.W., and Y.S.M.; Methodology, L.Y. and J.S.; Software, J.S.; Validation, L.Y., J.S., and J.-M.D.; Formal Analysis, L.Y. and J.S.; Investigation, L.Y., J.S., J.M., J.-M.D., C.R., V.L.L., and Y.Y.; Resources, J.O. and X.W.; Writing – Original Draft, L.Y., J.S., J.-M.D., Y.Y., J.O., X.W., J.W., and Y.S.M.; Writing – Review & Editing, L.Y., J.S., J.-M.D., J.O., J.W., and Y.S.M.; Visualization, L.Y. and J.S.; Supervision, J.W. and Y.S.M.; Project Administration, J.W. and Y.S.M.; Funding Acquisition, J.W. and Y.S.M.

DECLARATION OF INTERESTS

L.Y., J.S., J.W., and Y.S.M. are among the inventors of a provisional patent application related to this work.

Received: August 6, 2020
Revised: October 30, 2020
Accepted: November 10, 2020
Published: December 7, 2020

REFERENCES

1. Gong, S., and Cheng, W. (2017). Toward soft skin-like wearable and implantable energy devices. Adv. Energy Mater. *7*, 1700648.

2. Ray, T.R., Choi, J., Bandodkar, A.J., Krishnan, S., Gutruf, P., Tian, L., Ghaffari, R., and Rogers, J.A. (2019). Bio-integrated wearable systems: a comprehensive review. Chem. Rev. *119*, 5461–5533.

3. Yin, L., Seo, J.K., Kurniawan, J., Kumar, R., Lv, J., Xie, L., Liu, X., Xu, S., Meng, Y.S., and Wang, J. (2018). Highly stable battery pack via insulated, reinforced, buckling-enabled interconnect array. Small *14*, e1800938.

4. Xu, S., Zhang, Y., Cho, J., Lee, J., Huang, X., Jia, L., Fan, J.A., Su, Y., Su, J., Zhang, H., et al. (2013). Stretchable batteries with self-similar serpentine interconnects and integrated wireless recharging systems. Nat. Commun. *4*, 1543.

5. Weng, W., Sun, Q., Zhang, Y., He, S., Wu, Q., Deng, J., Fang, X., Guan, G., Ren, J., and Peng, H. (2015). A gum-like lithium-ion battery based on a novel arched structure. Adv. Mater. *27*, 1363–1369.

6. Huang, Y., Ip, W.S., Lau, Y.Y., Sun, J., Zeng, J., Yeung, N.S.S., Ng, W.S., Li, H., Pei, Z., Xue, Q., et al. (2017). Weavable, conductive yarn-based NiCo//Zn textile battery with high energy density and rate capability. ACS Nano *11*, 8953–8961.

7. Gaikwad, A.M., Zamarayeva, A.M., Rousseau, J., Chu, H., Derin, I., and Steingart, D.A. (2012). Highly stretchable alkaline batteries based on an embedded conductive fabric. Adv. Mater. *24*, 5071–5076.

8. Zamarayeva, A.M., Gaikwad, A.M., Deckman, I., Wang, M., Khau, B., Steingart, D.A., and Arias, A.C. (2016). Fabrication of a high-performance flexible silver–zinc wire battery. Adv. Electron. Mater. *2*, 1500296.

9. Li, H., Liu, Z., Liang, G., Huang, Y., Huang, Y., Zhu, M., Pei, Z., Xue, Q., Tang, Z., Wang, Y., et al. (2018). Waterproof and tailorable elastic rechargeable yarn zinc ion batteries by a cross-linked polyacrylamide electrolyte. ACS Nano *12*, 3140–3148.

10. Kumar, R., Shin, J., Yin, L., You, J.M., Meng, Y.S., and Wang, J. (2017). All-printed, stretchable Zn-Ag2O rechargeable battery via hyperelastic binder for self-powering wearable electronics. Adv. Energy Mater. *7*, 1602096.

11. Liu, W., Chen, Z., Zhou, G., Sun, Y., Lee, H.R., Liu, C., Yao, H., Bao, Z., and Cui, Y. (2016). 3D porous sponge-inspired electrode for stretchable lithium-ion batteries. Adv. Mater. *28*, 3578–3583.

12. Mackanic, D.G., Yan, X., Zhang, Q., Matsuhisa, N., Yu, Z., Jiang, Y., Manika, T., Lopez, J., Yan, H., Liu, K., et al. (2019). Decoupling of mechanical properties and ionic conductivity in supramolecular lithium ion conductors. Nat. Commun. *10*, 5384.

13. Mackanic, D.G., Chang, T.H., Huang, Z., Cui, Y., and Bao, Z. (2020). Stretchable electrochemical energy storage devices. Chem. Soc. Rev. *49*, 4466–4495.

14. Kaltenbrunner, M., Kettlgruber, G., Siket, C., Schwödiauer, R., and Bauer, S. (2010). Arrays of ultracompliant electrochemical dry gel cells for stretchable electronics. Adv. Mater. *22*, 2065–2067.

15. Li, H., Han, C., Huang, Y., Huang, Y., Zhu, M., Pei, Z., Xue, Q., Wang, Z., Liu, Z., Tang, Z., et al. (2018). An extremely safe and wearable solid-state zinc ion battery based on a hierarchical structured polymer electrolyte. Energy Environ. Sci. *11*, 941–951.

16. Song, W.-J., Lee, S., Song, G., and Park, S. (2019). Stretchable aqueous batteries: progress and prospects. ACS Energy Lett *4*, 177–186.

17. Ma, L., Chen, S., Wang, D., Yang, Q., Mo, F., Liang, G., Li, N., Zhang, H., Zapien, J.A., and Zhi, C. (2019). Super-stretchable zinc–air batteries based on an alkaline-tolerant dual-network hydrogel electrolyte. Adv. Energy Mater. *9*, 1803046.

18. Kim, J., Kumar, R., Bandodkar, A.J., and Wang, J. (2017). Advanced materials for printed wearable electrochemical devices: a review. Adv. Electron. Mater. *3*, 1600260.

19. Lanceros-Méndez, S., and Costa, C.M. (2018). Printed Batteries: Materials, Technologies and Applications (John Wiley & Sons).

20. Pan, H., Shao, Y., Yan, P., Cheng, Y., Han, K.S., Nie, Z., Wang, C., Yang, J., Li, X., Bhattacharya, P., et al. (2016). Reversible aqueous zinc/manganese oxide energy storage from conversion reactions. Nat. Energy *1*, 16039.

21. Lee, J.-S., Tai Kim, S., Cao, R., Choi, N.-S., Liu, M., Lee, K.T., and Cho, J. (2011). Metal-air batteries with high energy density: Li-air versus Zn-air. Adv. Energy Mater. *1*, 34–50.

22. Zeng, Y., Zhang, X., Meng, Y., Yu, M., Yi, J., Wu, Y., Lu, X., and Tong, Y. (2017). Achieving ultrahigh energy density and long durability in a flexible rechargeable quasi-solid-state Zn–MnO2 battery. Adv. Mater. *29*, 1700274.

23. Li, Y., Fu, J., Zhong, C., Wu, T., Chen, Z., Hu, W., Amine, K., and Lu, J. (2019). Recent advances in flexible zinc-based rechargeable batteries. Adv. Energy Mater. *9*, 1802605.

24. Yan, C., Wang, X., Cui, M., Wang, J., Kang, W., Foo, C.Y., and Lee, P.S. (2014). Stretchable silver-zinc batteries based on embedded nanowire elastic conductors. Adv. Energy Mater. *4*, 1301396.

25. Venkatraman, M., and Van Zee, J.W. (2007). A model for the silver–zinc battery during high rates of discharge. J. Power Sources *166*, 537–548.

26. Bonk, J.F., and Garrett, A.B. (1959). A study of the silver (I) oxide-silver (II) Oxide electrode. J. Electrochem. Soc. *106*, 612–615.

27. Takeda, K., and Hattori, T. (1999). Optimal process for fabricating AgO cathode for AgO/Zn cells improved in high drain pulse performance at low temperatures. J. Electrochem. Soc. *146*, 3190–3195.

28. Parkhurst, W.A., Dallek, S., and Larrick, B.F. (1984). Thermogravimetry-evolved gas analysis of silver oxide cathode material. J. Electrochem. Soc. *131*, 1739–1742.

29. Shin, J., You, J.M., Lee, J.Z., Kumar, R., Yin, L., Wang, J., and Shirley Meng, Y. (2016). Deposition of ZnO on bismuth species towards a rechargeable Zn-based aqueous battery. Phys. Chem. Chem. Phys. *18*, 26376–26382.

30. Xu, W., Wang, S.Q., Zhang, Q.Y., Ma, C.Y., Wang, Q., Wen, D.H., and Li, X.N. (2019). Hierarchically structured AgO films with nano-porosity for photocatalyst and all solid-state thin film battery. J. Alloys Compd. *802*, 210–216.

31. McMillan, J.A. (1962). Higher oxidation states of silver. Chem. Rev. *62*, 65–80.

32. Kumar, R., Johnson, K.M., Williams, N.X., and Subramanian, V. (2019). Scaling printable Zn–Ag2O batteries for integrated electronics. Adv. Energy Mater. *9*, 1803645.

33. Braam, K., and Subramanian, V. (2015). A stencil printed, high energy density silver oxide battery using a novel photopolymerizable poly(acrylic acid) separator. Adv. Mater. *27*, 689–694.

34. Choi, K.H., Ahn, D.B., and Lee, S.Y. (2018). Current status and challenges in printed batteries: toward form factor-free, monolithic integrated power sources. ACS Energy Lett. *3*, 220–236.

35. Entezam, M., Poormadadkar, H., Khonakdar, H.A., and Jafari, S.H. (2020). Melt rheology and interfacial properties of binary and ternary blends of PS, EOC, and SEBS. J. Appl. Polym. Sci. *137*, 48791.

36. Turney, D.E., Gallaway, J.W., Yadav, G.G., Ramirez, R., Nyce, M., Banerjee, S., Chen-Wiegart, Y.K., Wang, J., D'Ambrose, M.J., Kolhekar, S., et al. (2017). Rechargeable zinc alkaline anodes for long-cycle energy storage. Chem. Mater. *29*, 4819–4832.

37. Mainar, R.A., Leonet, O., Bengoechea, M., Boyano, I., de Meatza, I., Kvasha, A., Guerfi, A., and Alberto Blázquez, J. (2016). Alkaline aqueous electrolytes for secondary zinc–air batteries: an overview. Int. J. Energy Res. *40*, 1032–1049.

38. Braam, K.T., Volkman, S.K., and Subramanian, V. (2012). Characterization and optimization of a printed, primary silver–zinc battery. J. Power Sources *199*, 367–372.

39. Bandodkar, A.J., Hung, V.W.S., Jia, W., Valdés-Ramírez, G., Windmiller, J.R., Martinez, A.G., Ramírez, J., Chan, G., Kerman, K., and Wang, J. (2013). Tattoo-based potentiometric ion-selective sensors for epidermal pH monitoring. Analyst *138*, 123–128.

40. Yin, L., Kumar, R., Karajic, A., Xie, L., You, J., Joshuia, D., Lopez, C.S., Miller, J., and Wang, J. (2018). From all-printed 2D patterns to free-standing 3D structures: controlled buckling and selective bonding. Adv. Mater. Technol. *3*, 1800013.

41. Dellis, J.-L. (2020). Zfit. https://www.mathworks.com/matlabcentral/fileexchange/19460-zfit.

42. D'Errico, J. fminsearchbnd (2012). fminsearchcon. https://www.mathworks.com/matlabcentral/fileexchange/8277-fminsearchbnd-fminsearchcon.

43. Rustomji, C.S., Mac, J., Choi, C., Kim, T.K., Choi, D., Meng, Y.S., and Jin, S. (2016). Thin-film electrochemical sensor electrode for rapid evaluation of electrolytic conductivity, cyclic voltammetry, and temperature measurements. J. Appl. Electrochem. *46*, 59–67.

JOUL, Volume *5*

Supplemental Information

High Performance Printed AgO-Zn Rechargeable Battery for Flexible Electronics

Lu Yin, Jonathan Scharf, Jessica Ma, Jean-Marie Doux, Christopher Redquest, Viet L. Le, Yijie Yin, Jeff Ortega, Xia Wei, Joseph Wang, and Ying Shirley Meng

Supplemental Information

Supplemental Tables

Table S1. Comparison of areal capacities of various published and commercialized thick-film batteries. The summary is also visualized in **Figure S1**.

Battery Type	Fabrication	Max. Areal Capacity (mAh/cm^2)	Configuration	Cycle Number	Ref
Zn-Ag_2O	Screen Printing	1.6	In-plane	11	[1]
Zn-Ag_2O	Screen Printing	~3	In-plane	30	[2]
Zn-Ag_2O	Extrusion Printing	~2.8	In-plane	Primary	[3]
Zn-Ag_2O	Screen Printing	1.5	In-plane	13	[4]
Zn-MnO_2	Plotting	~2.2	In-plane	30	[5]
Zn-MnO_2	Doctor Blade	<0.077	Stacked	140	[6]
Zn-Ag_2O	Drop-cast/ Electroplating	0.11	In-Plane	33	[7]
Zn-MnO_2	Screen Printing	5.6	Stacked	Primary	[8]
Zn-Ag_2O	Screen Printing	5.4	Stacked	Primary	[9]
Zn-Ag_2O	3D Printing	2.4	Interdigitated Pillars	7	[10]
Zn-MnO_2	Soaking	3.775	In-plane	Primary	[11]
LTO-LFP	3D Printing	1.5	In plane Interdigitated	30	[12]
Zn-Air	Screen Printing	1.4	Stacked	Primary	[13]
Zn-Ag_2O	Screen Printing	11	Stacked	Primary	[14]
Si/CNT-NMC	Doctor Blade	30	Stacked	50	[15]
Zn-MnO_2	NA	~1	In-plane	Primary	[16]
Zn-MnO_2	NA	~3	NA	Primary	[17]
Zn-MnO_2	NA	~1.5	NA	Primary	[18]
Li-MnO_2	NA	~2.5	Stacked	Primary	[19]
AgO-Zn	Screen Printing	54	Stacked	80	This work

Table S2. KOH-PVA electrolyte information

Caustic Concentration	Removed Precursor Water wt%	σ_0 (mS/cm)	E_a (eV)
26.3%	65.77%	2.037×10^4	0.109
31.8%	70.72%	3.155×10^4	0.115
36.5%	73.88%	6.029×10^4	0.138

Table S3. Particle size distribution from material data sheet of the powder used.

	D10 (μm)	D50 (μm)	D90 (μm)	Avg. Size (μm)
Zn	1.5-2.0	2.5-3.5	5.0-6.0	/
AgO*	/	/	/	/
Cellulose	/	22	53	/
TiO_2	/	/	/	0.2

*: AgO particle distribution: >100 μm = <15%, 100-75 μm = 20-40%, 75-45 μm = 40-60%, <45 μm = <15%

Supplemental Figures

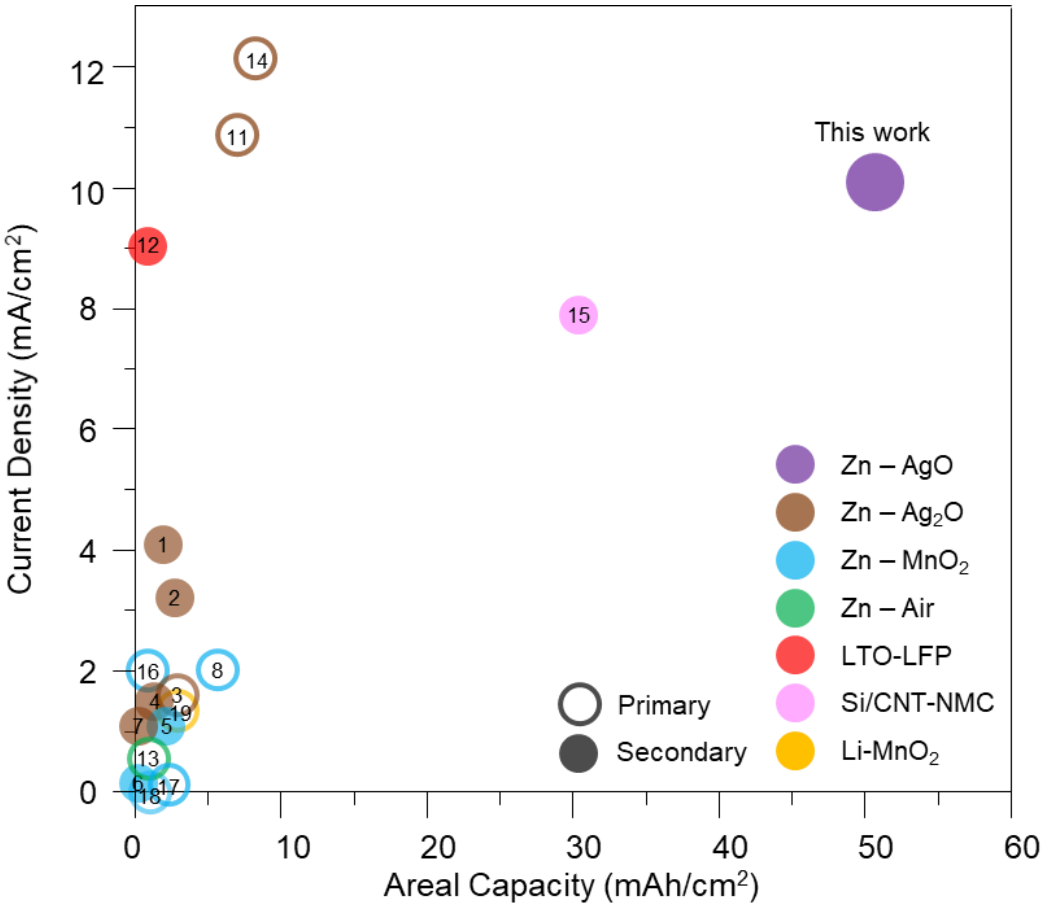

Figure S1. Visualization of **Table S1** comparing the maximum current densities and areal capacities of various printed batteries.

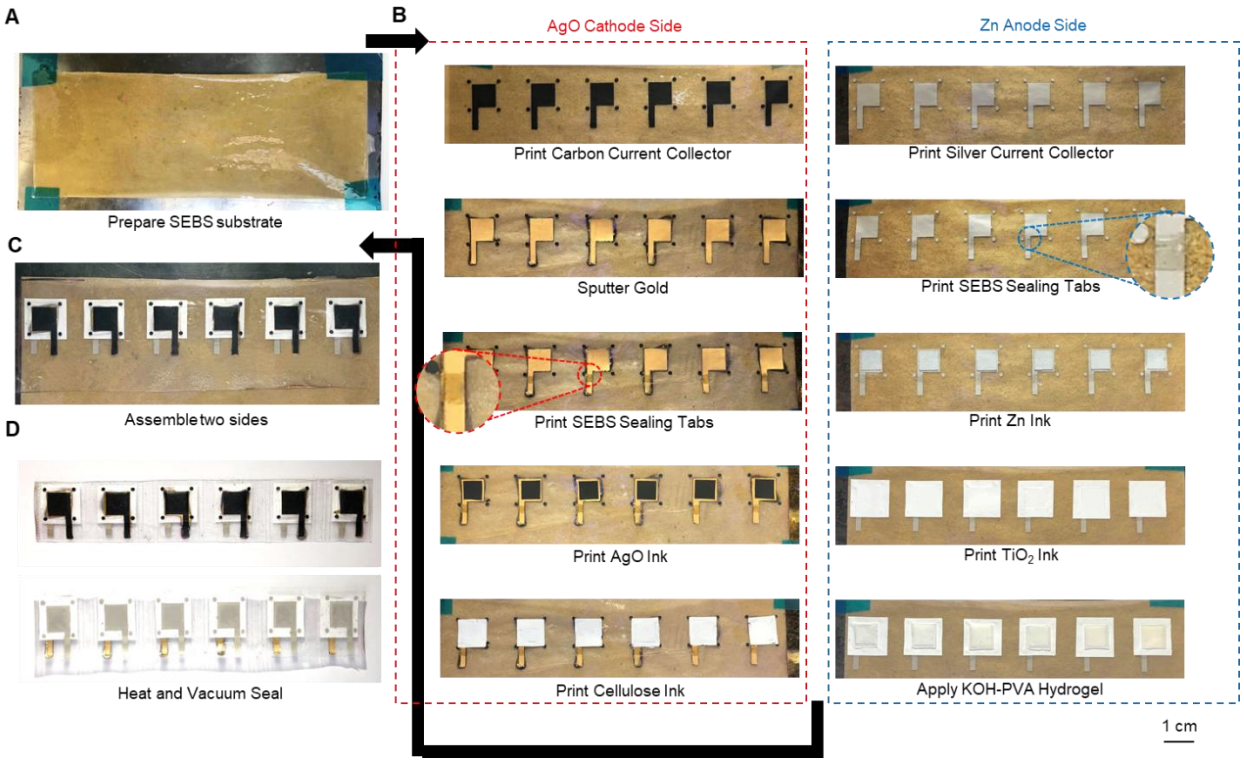

Figure S2. The images of the step-by-step batched fabrication of the printed AgO-Zn batteries. (A) Prepared SEBS substrate. (B) The layer-by-layer printing of the AgO cathode (left) and the Zn anode (right). (C) Placing the cathode side onto the anode side with the hydrogel electrolyte in between. (D) Heat and vacuum sealing of the batteries. Each cell was separated by further heat sealing after the entire batch was vacuum sealed.

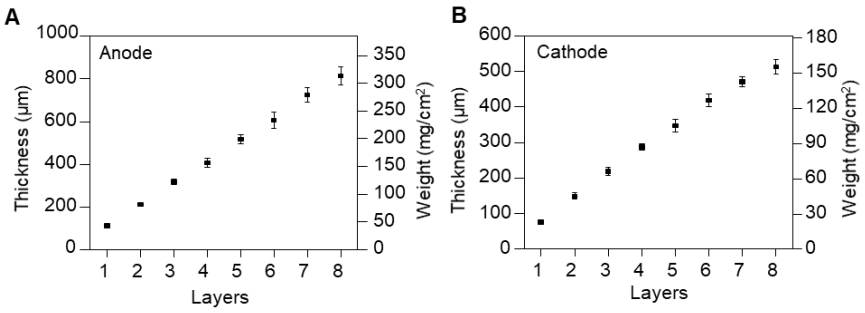

Figure S3. Thickness calibration of the (A) anode and (B) cathode printed using their corresponding stencils. 5 samples were taken to generate the average thicknesses and standard deviations of each data point.

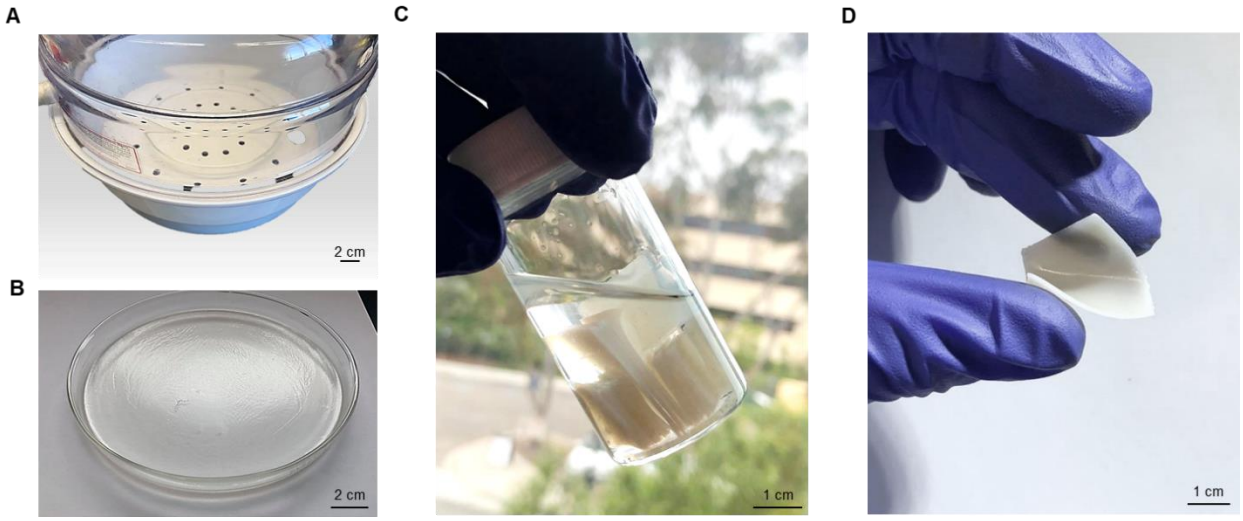

Figure S4. Images of the fabrication of the KOH-PVA electrolyte gel. (A) Drying of the precursor solution to desired concentration in a vacuum desiccator. (B) The crosslinked 36.5 % hydrogel after drying. (C) Storage of the hydrogel pieces after cutting into desired sizes. (D) A bent 2 × 2 cm^2 hydrogel.

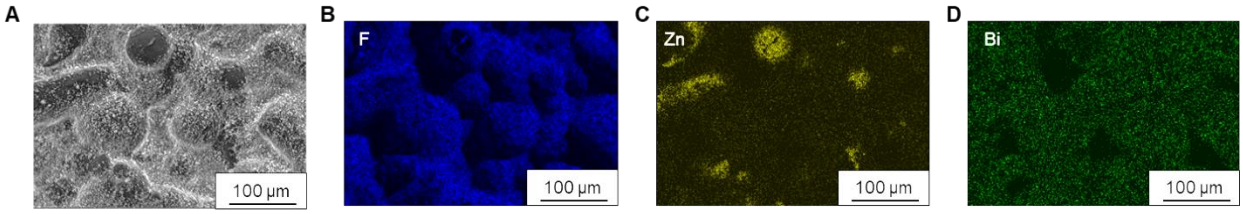

Figure S5. (A) The SEM and corresponding EDX mapping of (B) fluorine (from the binder), (C) Zn, and (D) bismuth of the anode.

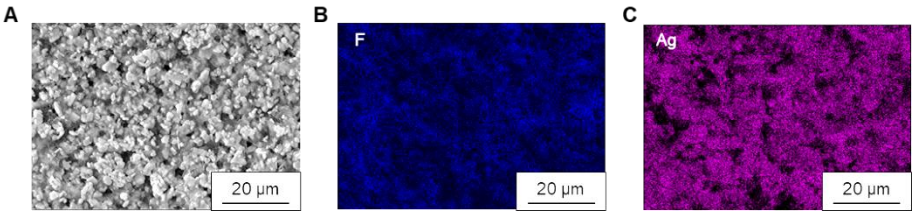

Figure S6 (A) The SEM and corresponding EDX mapping of (B) fluorine (from the binder) and (C) Ag of the cathode.

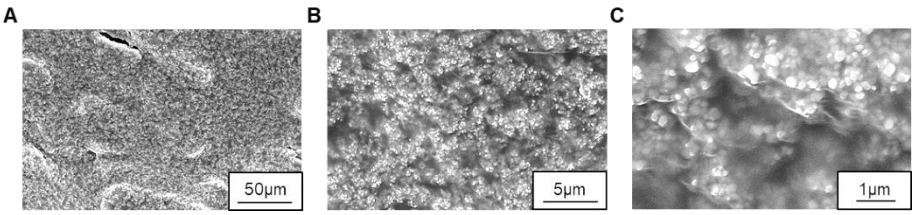

Figure S7. Additional SEM images of the printed TiO_2 separator with different magnifications.

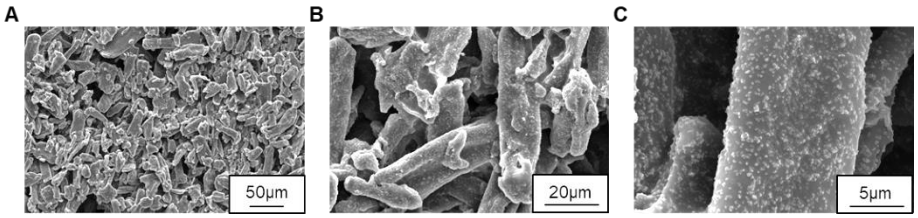

Figure S8. Additional SEM images of the printed cellulose separator with different magnifications.

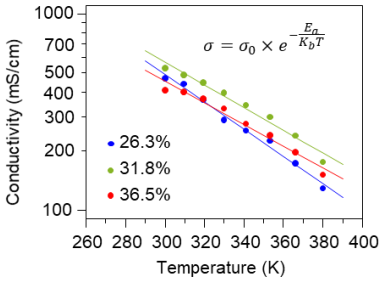

Figure S9. The conductivity of the hydrogel with different caustic material concentrations. The linear trendline was fitted using the given equation and listed in **Table S2**.

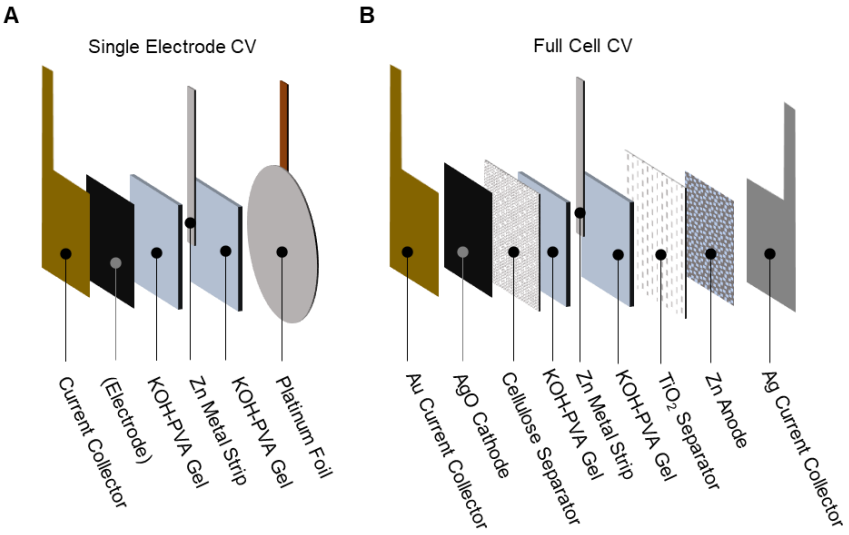

Figure S10. The cell structure used for the CV analysis. (A) The cell structure used for single electrode scanning for testing the current collectors. (B) The cell structure used for full cell scanning with an external Zn metal strip as the reference electrode.

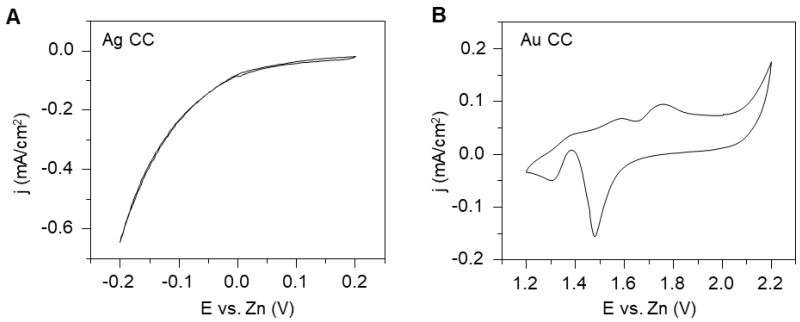

Figure S11. The CV of the printed (A) Ag anode current collector (CC) and the Au-sputtered carbon cathode CC in their corresponding voltage range used in **Figure 2D-ii**. Scan rate: 10 mV/s.

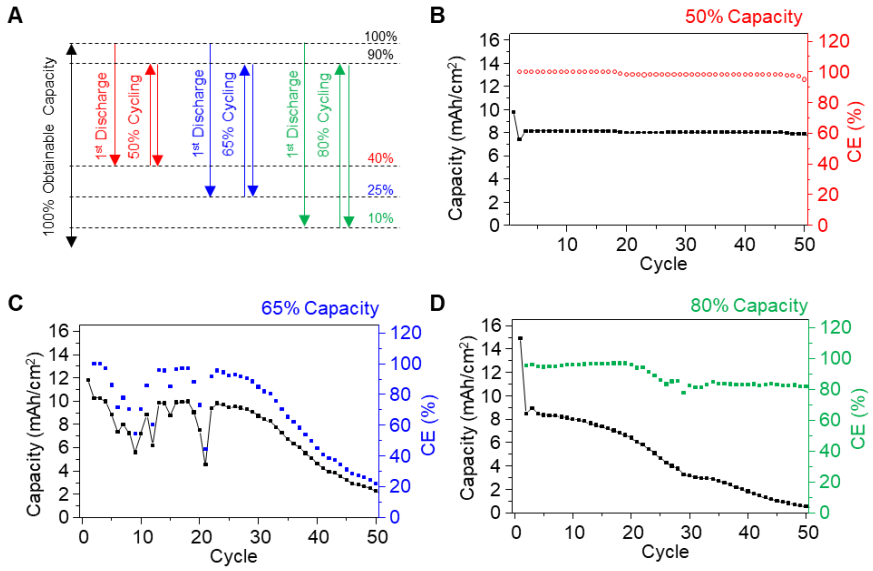

Figure S12. The cycling of the battery at the different capacity range. (A) The illustration comparing 3 different charging and discharging capacity regions. (B) Cycling the battery between 40 % and 90 % state of charge (50 %). (C) Cycling the battery between 25 % and 90 % state of charge (65 %). (D) Cycling the battery between 10 % and 90 % state of charge (80 %). Electrolyte with the concentration of 36.5 % was used, and the cells were cycled at the rate of 0.2 C.

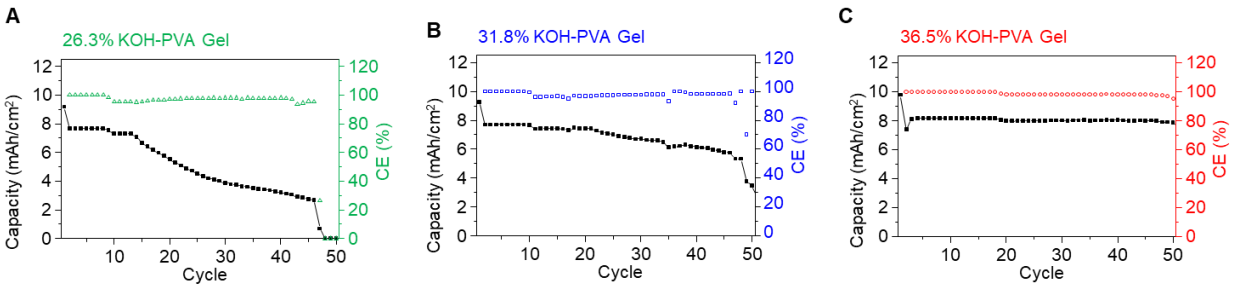

Figure S13. The cycling of the battery with electrolyte concentration of (A) 26.3 %, (B) 31.8 %, and (C) 36.5 %. The 50 % capacity range was used and the cells were cycled at the rate of 0.2 C.

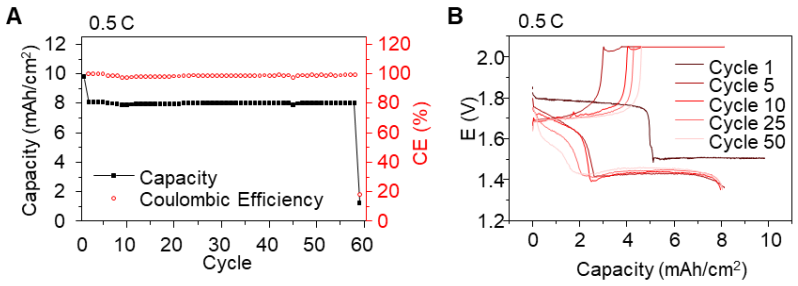

Figure S14. The cycling of the battery at the rate of 0.5 C. The electrolyte with the concentration of 36.5% and the capacity range of 50% was used.

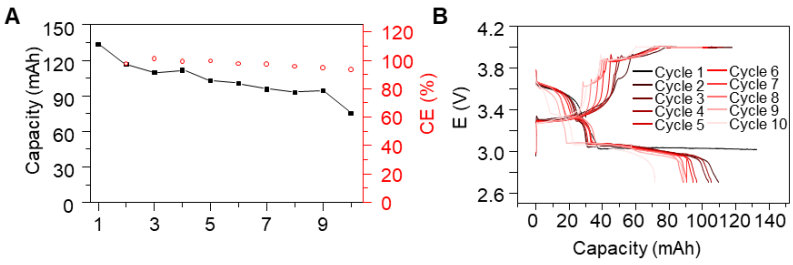

Figure S15. The cycling of two 8-layer 2 × 2 cm^2 battery connected in series at the rate of 0.05 C.

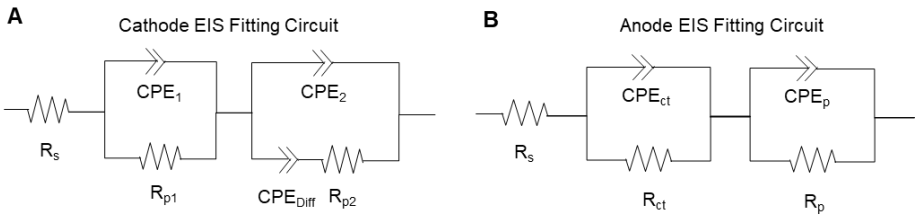

Figure S16. The equivalent circuit used for the (A) cathode and (B) anode EIS fitting.

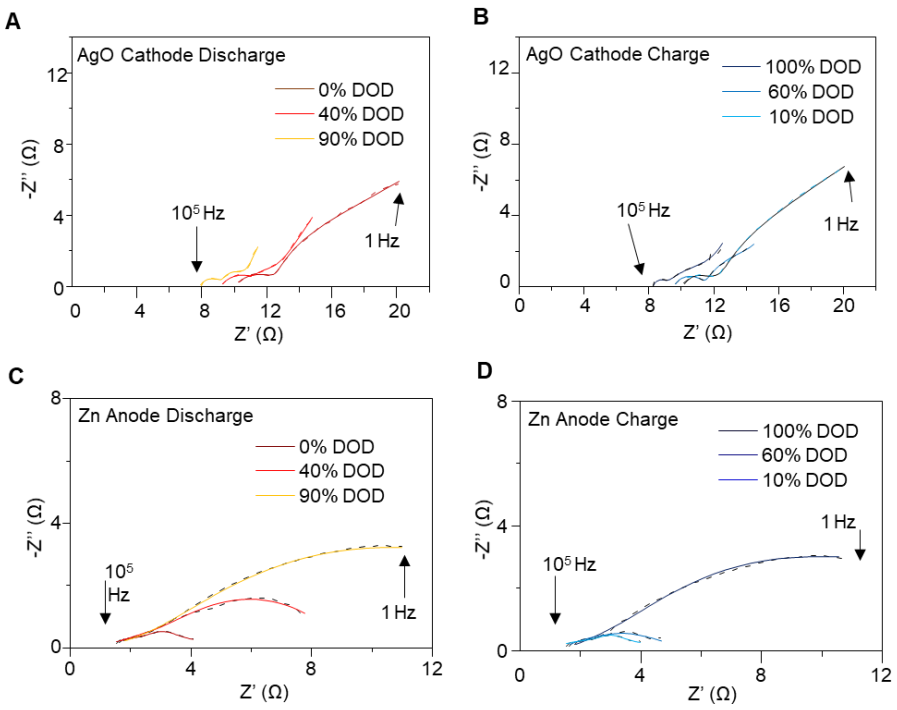

Figure S17. The Nyquist plot and the EIS fitting of the cathode during the 5th cycle (A) discharging and (B) charging, and the corresponding anode (C) charging and (D) discharging.

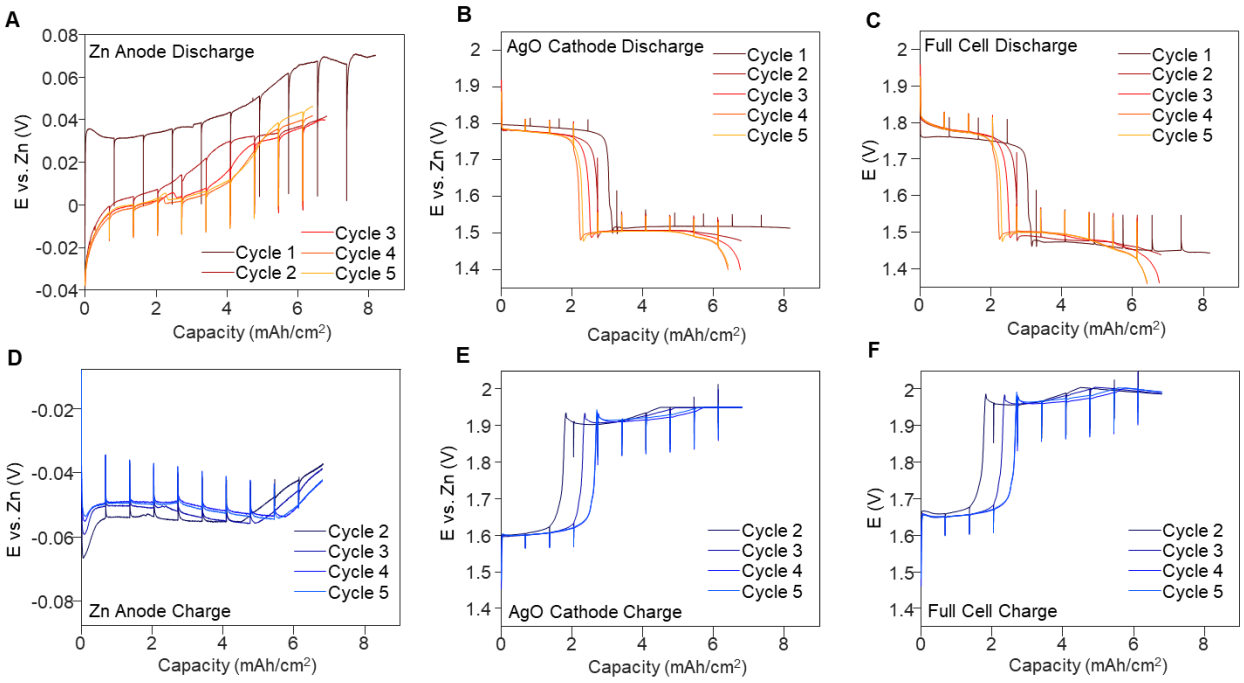

Figure S18. The potential profile of the anode (A,D) and cathode (B,E) vs. Zn reference and the full cell (C, F) within the first 5 cycles of (A-D) discharging and (D-F) corresponding 4 cycles of charging. The vertical lines correspond to the places where an EIS measurements were taken.

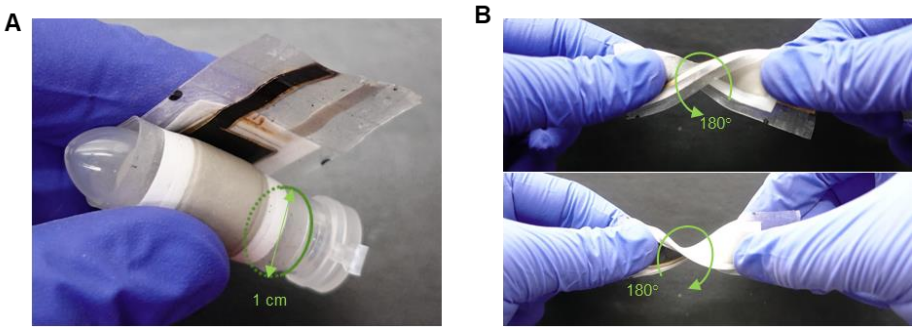

Figure S19. Additional images illustrating the manual bending and twisting of the battery. (A) A tube with diameter of 1 cm was used to bend the battery for half and one entire round. (B) The battery was twisted counterclockwise and clockwise 180° which add up to a total of 360°.

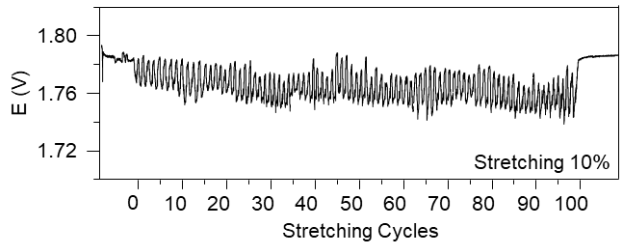

Figure S20. The voltage profile of the 1 × 5 cm^2 battery during 1 mA discharge while undergoing 100 cycles of 10 % lengthwise stretching. Although the battery was not optimized for stretchability, a certain amount of stretchability is required for the battery to endure low-radius bending and accommodate for the outer-layer strain.

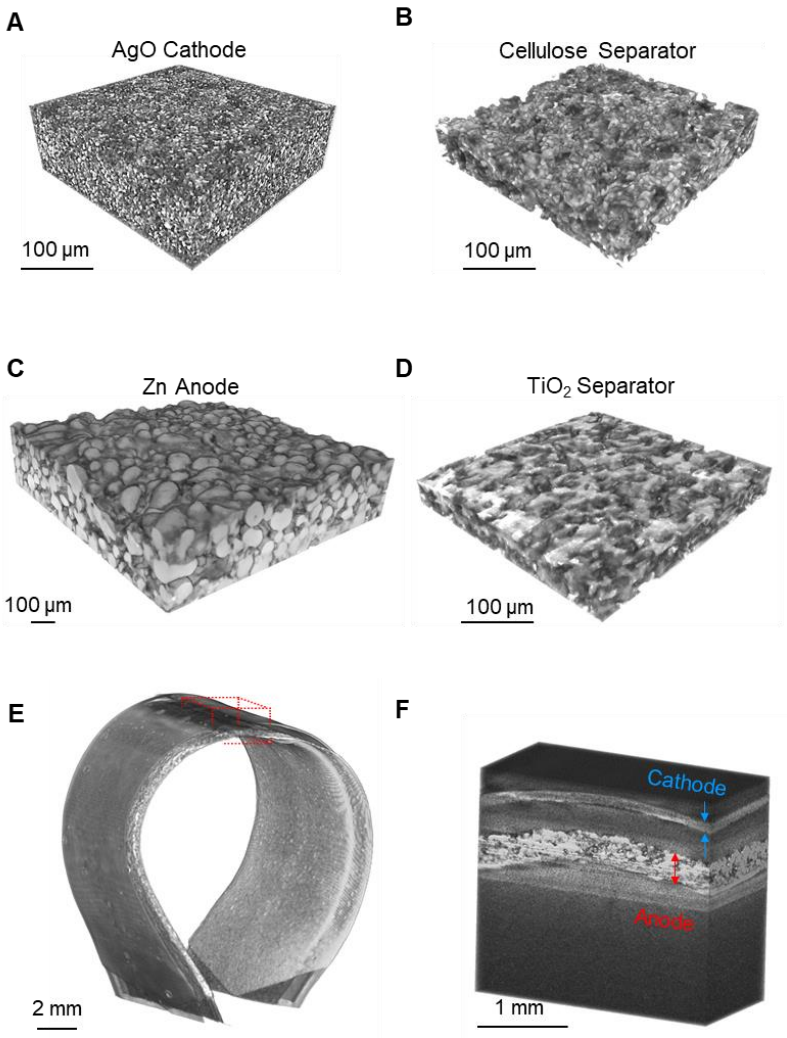

Figure S21. Additional microscopic 3D images of the (A) cathode, (B) cellulose separator, (C) anode, and (D) TiO_2 separator generated using the micro-CT. (E) the 3D image of the bent 1 × 5 cm^2 battery in a different angle and (F) the zoomed-in view of the top of the cell showing no cracking nor delamination between the layers.

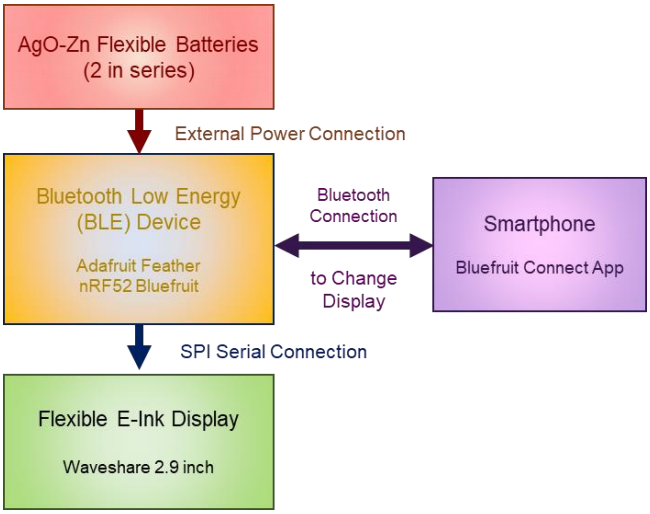

Figure S22.The system diagram of the assembled flexible E-ink display system.

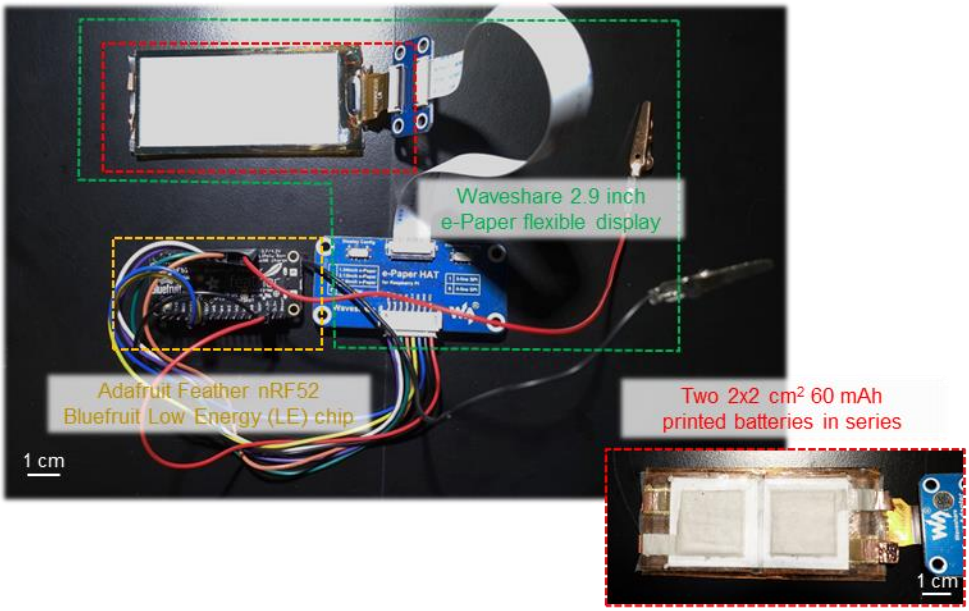

Figure S23. The photo of the assembled flexible E-ink display system with 2 batteries attached to the backside of the display panel.

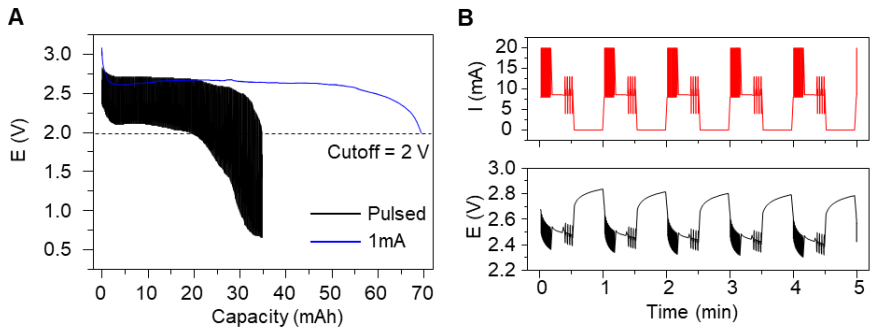

Figure S24. (A) The discharge curve of a CR1620 Lithium coin cell battery rated at 68 mAh nominal capacity under continuous 1 mA discharge and pulsed discharge.[20] Significant capacity fade is observed for the battery with pulsed discharge. (B) Zoomed in view of the current and voltage change of the CR1620 battery.

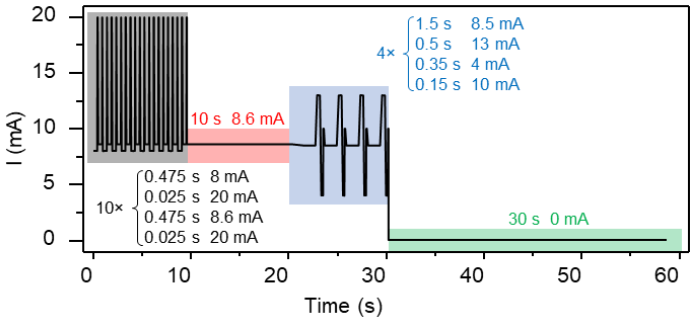

Figure S25. The detailed breakdown of the pulsed discharge profile.

Supplemental References

1. Wang, S.J., Meng, Y.S., Shin, J., You, J.-M., Lee, J.Z., Kumar, R., Yin, L., Wang, J., and Meng, S. (2016). Deposition of ZnO on bismuth species towards a rechargeable Zn-based aqueous battery. Phys. Chem. Chem. Phys *18*, 26376–26382.

2. Kumar, R., Shin, J., Yin, L., You, J.-M., Meng, Y.S., and Wang, J. (2017). All-Printed, Stretchable Zn-Ag2O Rechargeable Battery via Hyperelastic Binder for Self-Powering Wearable Electronics. Advanced Energy Materials *7*, 1602096.

3. Braam, K.T., Volkman, S.K., and Subramanian, V. (2012). Characterization and optimization of a printed, primary silver–zinc battery. Journal of Power Sources *199*, 367–372.

4. Berchmans, S., Bandodkar, A.J., Jia, W., Ramírez, J., Meng, Y.S., and Wang, J. (2014). An epidermal alkaline rechargeable Ag–Zn printable tattoo battery for wearable electronics. J. Mater. Chem. A *2*, 15788–15795.

5. Kettlgruber, G., Kaltenbrunner, M., Siket, C.M., Moser, R., Graz, I.M., Schwödiauer, R., and Bauer, S. (2013). Intrinsically stretchable and rechargeable batteries for self-powered stretchable electronics. J. Mater. Chem. A *1*, 5505–5508.

6. Winslow, R., Wu, C.H., Wang, Z., Kim, B., Keif, M., Evans, J., and Wright, P. (2013). Development and manufacture of printable next-generation gel polymer ionic liquid electrolyte for Zn/MnO2batteries. J. Phys.: Conf. Ser. *476*, 012085.

7. Yan, C., Wang, X., Cui, M., Wang, J., Kang, W., Foo, C.Y., and Lee, P.S. (2014). Stretchable Silver-Zinc Batteries Based on Embedded Nanowire Elastic Conductors. Advanced Energy Materials *4*, 1301396.

8. Gaikwad, A.M., Whiting, G.L., Steingart, D.A., and Arias, A.C. (2011). Highly Flexible, Printed Alkaline Batteries Based on Mesh-Embedded Electrodes. Advanced Materials *23*, 3251–3255.

9. Braam, K., and Subramanian, V. (2015). A Stencil Printed, High Energy Density Silver Oxide Battery Using a Novel Photopolymerizable Poly(acrylic acid) Separator. Advanced Materials *27*, 689–694.

10. Ho, C.C., Murata, K., Steingart, D.A., Evans, J.W., and Wright, P.K. (2009). A super ink jet printed zinc–silver 3D microbattery. J. Micromech. Microeng. *19*, 094013.

11. Gaikwad, A.M., Zamarayeva, A.M., Rousseau, J., Chu, H., Derin, I., and Steingart, D.A. (2012). Highly Stretchable Alkaline Batteries Based on an Embedded Conductive Fabric. Advanced Materials *24*, 5071–5076.

12. Sun, K., Wei, T.-S., Ahn, B.Y., Seo, J.Y., Dillon, S.J., and Lewis, J.A. (2013). 3D Printing of Interdigitated Li-Ion Microbattery Architectures. Advanced Materials *25*, 4539–4543.

13. Hilder, M., Winther-Jensen, B., and Clark, N.B. (2009). Paper-based, printed zinc–air battery. Journal of Power Sources *194*, 1135–1141.

14. Kumar, R., Johnson, K.M., Williams, N.X., and Subramanian, V. (2019). Scaling Printable Zn–Ag2O Batteries for Integrated Electronics. Advanced Energy Materials *9*, 1803645.

15. Park, S.-H., King, P.J., Tian, R., Boland, C.S., Coelho, J., Zhang, C. (John), McBean, P., McEvoy, N., Kremer, M.P., Daly, D., et al. (2019). High areal capacity battery electrodes enabled by segregated nanotube networks. Nature Energy *4*, 560–567.

16. Blue Spark Battery Products https://www.bluesparktechnologies.com/index.php/products-and-services/battery-products/ultra-thin-series.

17. Enfucell Soft Battery Data Sheet https://asiakas.kotisivukone.com/files/enfucell.kotisivukone.com/Dokumentit/Enfucell_Soft Battery_specifications_2019-05-15.pdf.

18. Imprint Energy ZincPoly 8349 Battery Specification https://www.imprintenergy.com/s/Imprint-Energy-ZincPoly-8349-Battery-Datasheet-Rev22.pdf.

19. BrightVolt 452229-14XT Data Sheet https://www.brightvolt.com/wp-content/uploads/2018/06/452229-14XT.pdf.

20. Renata CR1620 Li Battery Data Sheet https://www.renata.com/fileadmin/downloads/productsheets/lithium/3V_lithium/CR1620.pdf.